Computers and Geotechnics 159 (2023) 105466

Contents lists available at ScienceDirect

Computers and Geotechnics

journal homepage: www.elsevier.com/locate/compgeo

A dynamic SNS-PFEM with generalized-α method for hydro-mechanical coupled geotechnical problems

Ze-Yu Wang [a,b,c], Yin-Fu Jin [a,*], Zhen-Yu Yin [b], Yu-Ze Wang [c]

[a] College of Civil and Transportation Engineering, Shenzhen University, Shenzhen 518060, Guangdong, China
[b] Department of Civil and Environmental Engineering, The Hong Kong Polytechnic University, Hung Hom, Kowloon, Hong Kong, China
[c] Department of Ocean Science and Engineering, Southern University of Science and Technology, Shenzhen, Guangdong, China

ARTICLE INFO

Keywords:
Node-based gradient smoothing
Hydro-mechanical coupling
Generalized-α method
Integration stabilization
Polynomial pressure projection

ABSTRACT

The node-based smoothed particle finite element method (NS-PFEM) is computationally efficient with pure linear interpolation, while some intrinsic defects hinder its application in dynamic and hydro-mechanical coupled analysis. This study proposes a dynamic implicit stable NS-PFEM (SNS-PFEM) with some features: (1) the subdomain-based stress point stabilization is applied to overcome the spurious non-zero energy mode of NS-PFEM; (2) the polynomial pressure projection is implemented into the dynamic SNS-PFEM to guarantee the pore pressure stabilization; (3) the implicit time marching scheme of generalized-α method to integrate the stabilized equations is derived, which is error-controllable, unconditionally stable regardless of time step and permeability; and (4) an updated Lagrangian remeshing scheme is implemented to deal with the large deformation. The proposed implicit SNS-PFEM is first validated by several benchmark examples, and then applied to analyse the seabed under wave loading, the cutting slope experiment, and the slope failure under seismic loading. All results demonstrate the proposed method is stable and accurate in modelling the hydro-mechanical coupled dynamic problems under small and large deformation with nonlinear soil constitutive models and different drainage conditions.

1. Introduction

Investigating the dynamic effects of the saturated soil is always essential and challenging in analysing practical geotechnical problems, such as the responses of seabed under waves and currents (Jeng et al., 2013; Ye and Jeng, 2011), the surface penetration with dynamic loading (Kim et al., 2015; Sabetamal et al., 2014; Sabetamal et al., 2016), the wave propagation in the saturated field (Kontoe et al., 2008; Markert et al., 2010), to name a few. The mutual interaction of soil skeleton and pore fluids could be particularly significant in the seismic-induced geohazards, since the shaking of ground base could rapidly increase the pore pressure and lead to the abrupt loss of the strength of saturated soil with structure collapsing, which is commonly termed as liquefaction (Li et al., 2004; Markert et al., 2010; Ye and Jeng, 2012). Furthermore, most of the aforementioned problems are also accompanied with large deformation and highly nonlinear behaviours of soil, which pose huge difficulties in the numerical simulations. Therefore, it is of great value to develop accurate and efficient numerical tools for the dynamic analysis of two-phase geotechnical problems with large deformation.

Mathematical models of hydro-mechanical coupled dynamics in porous medium have long been developed. Biot extended the classical consolidation equations to coupled dynamic theory by introducing the inertia terms of the soil skeleton and pore fluids (Biot, 1956a; Biot, 1956b; Biot, 1962). It was then improved to consider the compressibility of solids and acceleration convective term of fluids (Zienkiewicz et al., 1980). The full Biot dynamic model can be formulated as several formats (Monforte et al., 2019; Yuan et al., 2022; Zienkiewicz and Shiomi, 1984), i.e., *u-U*, *u-w-p*, and *u-U-p* (where *u* is the solid displacement, *U* the fluid displacement, *w* the fluid velocity and *p* the pore pressure.). These formulations are widely applicable in conditions with both low-frequency and high-frequency dynamic loading (Zienkiewicz and Shiomi, 1984). However, they are all computationally expensive because each node carries 4–5 degrees of freedom in 2D conditions, i.e., two additional displacement or velocity components of the fluid phase. The most popular format used in geotechnical practice is the reduced *u-p* formulation with only 3 degrees of freedom of each node (Xu et al.,

* Corresponding author.
E-mail addresses: ze-yu.wang@connect.polyu.hk (Z.-Y. Wang), yinfujin@szu.edu.cn (Y.-F. Jin), zhenyu.yin@polyu.edu.hk (Z.-Y. Yin), wangyz@sustech.edu.cn (Y.-Z. Wang).

https://doi.org/10.1016/j.compgeo.2023.105466
Received 7 December 2022; Received in revised form 4 April 2023; Accepted 6 April 2023
Available online 24 April 2023

2017a; Xu et al., 2017b; Yuan et al., 2022; Zienkiewicz and Shiomi, 1984), which neglects the relative acceleration between solid and fluid phases. It is attractive in its applicable range due to the simple formulations and less computational cost. Besides, the *u-p* formulation has been proven sufficient to deal with most of the conventional geotechnical dynamic problems, e.g., the problems with ocean wave and earthquake loading (Monforte et al., 2019; Xu et al., 2017a; Ye and Jeng, 2012; Zienkiewicz and Shiomi, 1984), and also the problems involving soil-structure interaction (Carbonell et al., 2022; Monforte et al., 2018; Sabetamal et al., 2021).

There is still an intrinsic flaw endangering the numerical stability of *u-p* format, that is, the spurious pore pressure oscillations due to the violation of the inf-sup Ladyzhenskaya-Babuška-Brezzi (LBB) condition (Brezzi and Bathe, 1990; White and Borja, 2008). This problem is especially significant in the undrained limit with equal-order interpolation for u and p. Fortunately, numerous stabilization techniques have been developed for Galerkin-type numerical frameworks, including the separate interpolations for coupled variables (Haga et al., 2012), finite-incremental calculus (FIC) (Onate, 2000; Preisig and Prevost, 2011), polynomial pressure projection (PPP) (Wang et al., 2022a; Wei et al., 2016; White and Borja, 2008; Zhao and Choo, 2020), fractional step methods (Pastor et al., 2000), enhanced strain formulations (Mira et al., 2003), to name a few. Among them, the polynomial pressure projection has remarkable advantages in its solid theoretical foundation and convenience of implementation into the existing code as a plug-in (Mira et al., 2003; Wang et al., 2022a; White and Borja, 2008; Zhang et al., 2022a, 2022b). It has been successfully applied in a wide range of hydro-mechanical coupled numerical methods (Wang et al., 2022a; Wei et al., 2016; White and Borja, 2008; Zhang et al., 2021; Zhao and Choo, 2020), including the dynamic condition with low-order *u-p* element in FEM (Monforte et al., 2019).

On the other hand, numerous numerical methods have been developed for the geotechnical simulations with dynamics and large deformation, which can be categorized into two branches: the mesh-based methods, including the Arbitrary Lagrangian-Eulerian scheme (ALE) (Sabetamal et al., 2014), the material point methods (MPM) (Andersen and Andersen, 2010; Soga et al., 2016; Yerro et al., 2015), and the particle finite element method (PFEM) (Wang et al., 2021a, 2021b); the meshfree-based methods, such as the smoothed particle hydrodynamics (SPH) (Bui and Fukagawa, 2013; Bui and Nguyen, 2017) and other meshfree Galerkin methods (Chen et al., 2001; Puso et al., 2008; Wei et al., 2020). The meshfree-based methods have great flexibility with the huge variation of geometry, whereas there are still some intrinsic drawbacks such as the difficulty of enforcing the essential boundary conditions (Chen et al., 2017; Liu, 2009), more complex quadrature rules for high-order interpolation, etc (Belytschko et al., 1994; Belytschko et al., 1996; Chen et al., 2001; Puso et al., 2008). The PFEM is developed to combine the deformation ability of meshfree methods and the rigorous mathematical bases of FEM (Cremonesi et al., 2020; Monforte et al., 2017a, 2017b; Wang et al., 2021a, 2021b; Zhang et al., 2015; Zhang et al., 2022a, 2022b). It uses an updated Lagrangian framework by rebuilding the mesh frequently with incremental displacement, where the severely distorted elements can be automatically eliminated. However, the traditional PFEM still has some drawbacks. For example, the pure linear element used in the *u-p* format could incur volumetric locking and spurious pore pressure oscillations requiring the special treatments (Hughes, 2000; Monforte et al., 2019). Although the mixed element (3-node for pore pressure and 6-node for displacement) is free of the aforementioned problems and accurate with complex soil constitutive models (Sabetamal et al., 2022; Sabetamal et al., 2021; Wang et al., 2021a, 2021b; Zhang et al., 2022a, 2022b), the computational cost is relatively huge due to the increased degrees of freedom and high-order interpolation (Wang et al., 2022a). Besides, the variable mapping between the quadrature points and nodes are needed for each remeshing process for PFEM with T6 element (Jin et al., 2020a, 2020b; Zhang et al., 2022a, 2022b), which can be avoided by using the PFEM with T3 element and node-based strain smoothing method while preserving the high accuracy without volumetric locking.

The strain-smoothing techniques are then developed, aiming to preserve the pure linear interpolation while overcome its defects, leading to some new methods such as the edge-based smoothed PFEM (ES-PFEM) (Jin et al., 2020a, 2020b; Nguyen-Xuan and Liu, 2013) and node-based smoothed PFEM (NS-PFEM) (Yuan et al., 2019; Zhang et al., 2018). Recently, the NS-PFEM is popular in geotechnical simulation because it is free from variable mapping and volumetric locking (Zeng and Liu, 2018). It has been proved that the node-based smoothed FEMs give larger displacement in the force driving problems than FEM, and this softening effect will increase as the number of smoothing domains decreases (Liu et al., 2010). The NS-PFEM is "overly soft", which gives softer response than the true solution, because the number of nodes is always smaller than that of elements and edges in a triangular mesh (Zeng and Liu, 2018). This feature can cause spuriously oscillated solutions in hydro-mechanical coupled analysis (Wang et al., 2022a). For the dynamic problems with NS-PFEM, the eigenvalues of stiffness matrix will be reduced to be lower than that of the mass matrix, which is named the spurious non-zero energy mode (Puso et al., 2008). This mode can lead to obvious deterioration in numerical stability and accuracy (Chen et al., 2001; Jin and Yin, 2022; Puso et al., 2008). Two types of integration stabilization remedies can be considered to solve the "overly soft" drawback and spurious non-zero energy mode of NS-PFEM, leading to the stable node-based smoothed PFEM (SNS-PFEM). One is the strain gradient stabilization, which assumes that the strain is linearly distributed in a circle domain centered on the node and the stress is evaluated on four quadrature points (Feng et al., 2016; Li and Liu, 2019; Vo-Minh and Nguyen-Son, 2021; Yang et al., 2019). The other is the subdomain-based stress point stabilization, which uses the subdomain-smoothed gradients evaluated on several additional stress points to augment the smoothed weak forms (Chen et al., 2001; Puso et al., 2008; Wang et al., 2022a). The latter is computationally more efficient for NS-PFEM, because the subdomain-smoothed gradient is just the compatible gradient calculated beforehand for linear shape function, and thus no extra computational effort is required. Some recent studies have developed the explicit NS-PFEM for dynamic analysis of saturated porous medium (Jin and Yin, 2022; Yuan et al., 2022), and the strain gradient technique is used to stabilize the temporal oscillations (Jin and Yin, 2022). The explicit scheme is always conditionally stable, which is difficult to handle the large time step and low-permeability conditions (Jin and Yin, 2022; Soga et al., 2016; Xu et al., 2017a). It is necessary to further develop a SNS-PFEM with implicit time marching scheme for the hydro-mechanical coupled dynamics, so as to be error-controllable and unconditionally stable with wider choice of time step.

This study is developed based on the implicit quasi-static SNS-PFEM (Wang et al., 2022a). The paper is organized as follows. In Sections 2.1 and 2.2, the strong and weak forms of the governing equations for dynamics in the porous medium, together with the formulations of polynomial pressure projection, are presented. Section 2.3 introduces the node-based smoothed method and subdomain-based stress point stabilization technique. Section 2.4 gives a detailed derivation of the step-by-step time integration algorithm with the CH generalized-α method (Han et al., 2015; Kontoe et al., 2008). Section 2.5 briefly illustrates the remeshing scheme for large deformation and the whole computational circle of the proposed SNS-PFEM. In Section 3, several benchmark examples are simulated to validate the accuracy and efficiency of SNS-PFEM together with some reference solutions. The effects of PPP and nodal integration stabilization are highlighted by comparison. In Section 4, three problems with more realistic geotechnical features and large deformation are calculated to demonstrate the ability of the method, including the seabed under wave loading, the Selborne slope experiment, and the slope failure under seismic loading.

2. SNS-PFEM for hydro-mechanical coupled dynamics

2.1. Governing equations and spatial discretization

The "*u-p*" formulation is adopted for the dynamic analysis of saturated porous medium, where the inertia term uses the density of mixture and neglects the small relative acceleration between fluid and solid skeleton. The momentum equilibrium equation including the inertia term is presented in Eq. (1). The mass conservation equation is exhibited in Eq. (2), where the fluid is simplified to be incompressible. The other governing laws of the effective stress principle and Darcy's law are presented in Eq. (3) and (4) respectively:

$$\nabla\cdot\boldsymbol{\sigma} - \rho\ddot{\boldsymbol{u}} + \boldsymbol{f} = \boldsymbol{0} \tag{1}$$

$$\nabla\cdot\dot{\boldsymbol{u}} + \nabla\cdot\widetilde{\boldsymbol{v}} = 0 \tag{2}$$

$$\boldsymbol{\sigma}' = \boldsymbol{\sigma} + p\boldsymbol{I} \tag{3}$$

$$\widetilde{\boldsymbol{v}} = -\frac{\boldsymbol{k}}{\rho_f g}\cdot\nabla p \tag{4}$$

where $\boldsymbol{\sigma}'$ is the effective stress tensor, $\boldsymbol{I}$ the identity tensor, $\boldsymbol{f}$ the body force in the medium, $\widetilde{\boldsymbol{v}}$ the Darcy velocity of fluid flux, ρ_f the density of fluid, g the gravity acceleration, $\boldsymbol{k}$ the hydraulic conductivity tensor, $\boldsymbol{u}$ the solid displacement field, and p the fluid pressure. The $\boldsymbol{u}$ and p are the driven variables in the governing equations and also act as the nodal variables in the final finite element formulations.

The definition of infinitesimal strain and the rate-form constitutive equation are written as Eqs. (5)–(6), with $\mathbb{D}_{ep}$ the elastoplastic modulus tensor. The natural and essential boundary conditions for the solid and fluid components are exhibited in Eq. (7) and (8) respectively:

$$\boldsymbol{\varepsilon} = \nabla^s\boldsymbol{u} = \frac{1}{2}(\nabla\boldsymbol{u} + \nabla\boldsymbol{u}^T) \tag{5}$$

$$\frac{d}{dt}\boldsymbol{\sigma}' = \mathbb{D}_{ep} : \frac{d}{dt}\boldsymbol{\varepsilon} \tag{6}$$

$$\begin{cases} \boldsymbol{u} - \overline{\boldsymbol{u}} = \boldsymbol{0} \text{ on } \Gamma_u \\ \boldsymbol{n}\cdot\boldsymbol{\sigma} - \overline{\boldsymbol{t}} = \boldsymbol{0} \text{ on } \Gamma_t \\ \Gamma = \Gamma_u \cup \Gamma_t,\ \Gamma_u \cap \Gamma_t = \varnothing \end{cases} \tag{7}$$

$$\begin{cases} p - \overline{p} = 0 \text{ on } \Gamma_p \\ \boldsymbol{n}\cdot\widetilde{\boldsymbol{v}} + \overline{q} = 0 \text{ on } \Gamma_q \\ \Gamma = \Gamma_p \cup \Gamma_q,\ \Gamma_p \cap \Gamma_q = \varnothing \end{cases} \tag{8}$$

where $\overline{\boldsymbol{u}}$ is the given displacement, $\overline{\boldsymbol{t}}$ the traction force, $\overline{p}$ the given pore pressure, and $\overline{q}$ the flow flux on the boundary.

Following the standard procedures of Galerkin method, the finite element equations of hydro-mechanical coupled dynamics can be written as the Eq. (9),

$$\begin{cases} \mathscr{L}_u^h = \boldsymbol{M}\ddot{\boldsymbol{U}} + \boldsymbol{C}\dot{\boldsymbol{U}} + \boldsymbol{F}^{ints}(\boldsymbol{U}) - \boldsymbol{K}_{up}\boldsymbol{P} - \boldsymbol{F}^{ext} = 0 \\ \mathscr{L}_p^h = \boldsymbol{K}_{up}^T\dot{\boldsymbol{U}} + \boldsymbol{K}_{pp}\boldsymbol{P} - \boldsymbol{Q}^{ext} = 0 \end{cases} \tag{9}$$

where **U** is the nodal displacement, **P** the nodal pore pressure, **M** the mass matrix, $\boldsymbol{K}_{uu}$ the stiffness matrix, $\boldsymbol{K}_{pp}$ the permeability matrix, $\boldsymbol{K}_{up}$ the coupling matrix, $\boldsymbol{C}$ the damping matrix, $\boldsymbol{F}^{ext}$ the external load vector and $\boldsymbol{Q}^{ext}$ the flow flux term. Note that the compressibility of fluid is neglected, as shown in Eqs. (2) and (9). The number of dots at the top of variables denotes the order of derivative to time. This is a group of second-order time-dependent ordinary differential equations of the nodal displacement and pore pressure. The detailed formulations and explanations of each term are summarized in Appendix A. The key points in the detailed derivation, including the weak form and spatial discretization, can be found in several preceding studies concerning the FEM of fully coupled Biot's consolidation. For the subsequent construction of node-based smoothed PFEM, the linear triangular element (T3) is chosen for both the displacement and the pore pressure, although Eq. (9) is independent of the choice of interpolation scheme.

2.2. Polynomial pressure projection (PPP)

It is well-known that the equal-order linear interpolation for displacement and pressure can incur severer numerical instability in the undrained limit due to the violation of the discrete inf-sup condition (Brezzi and Bathe, 1990; White and Borja, 2008). Some recent studies revealed that this problem plagued the coupled quasi-static NS-PFEM (Wang et al., 2022a). Section 3.2 in this study illustrates that spurious pressure oscillation is also significant in coupled dynamic problems. The polynomial pressure projection (PPP) offers an efficient remedy within the pure T3-based interpolation. It can be easily formulated as a plug-in to the permeability matrix without modifying the remaining code.

The stabilized mass conservation weak form of PPP is presented in Eq. (10), with the polynomial pressure projection term **S** defined in Eq. (11). The operator $\prod$ is defined in Eq. (12), where $\boldsymbol{x}$ is the spatial coordinates. $\prod$ projects the piecewise linear shape function to a piecewise constant function space, which makes the modified equation meet the weak inf-sup conditions. In this study, Ω_e is the element domain, and V_e is the element area. The detailed theories and proofs can be found in the preceding works (Brezzi and Bathe, 1990; Choo and Borja, 2015; White and Borja, 2008; Zhang et al., 2021). A simplified nodal integration formulation of the term **S** consistent with the node-based smoothed FEM can also be found in our previous paper (Wang et al., 2022a).

$$\begin{aligned} \mathscr{L}_{p,stab}^h &= \mathscr{L}_p^h + \int_\Omega \varepsilon_f \left[\boldsymbol{N}^p - \prod\boldsymbol{N}^p\right]^T \frac{\partial}{\partial t}\left[p^h - \prod p^h\right] d\boldsymbol{x} \\ &= \boldsymbol{K}_{up}^T\dot{\boldsymbol{U}} + \boldsymbol{K}_{pp}\boldsymbol{P} + \boldsymbol{S}\dot{\boldsymbol{P}} - \boldsymbol{Q}^{ext} = 0 \end{aligned} \tag{10}$$

$$\boldsymbol{S} = \int_\Omega \varepsilon_f \left[\boldsymbol{N}^p - \prod\boldsymbol{N}^p\right]^T \left[\boldsymbol{N}^p - \prod\boldsymbol{N}^p\right] d\boldsymbol{x} \tag{11}$$

$$\prod p^h(\boldsymbol{x})|_{\Omega_e} = \frac{1}{V_e}\int_{\Omega_e} p^h(\boldsymbol{x}) d\boldsymbol{x} \tag{12}$$

The polynomial pressure projection coefficient ε_f is determined using the technique proposed by (Sun et al., 2013), including an additional assumption of incompressibility of fluid and solid grains, as shown in Eqs. (13)–(14),

$$\varepsilon_f = \frac{1}{K + 4G/3}\left\langle 1 - 3\frac{c_w\Delta t}{h^2}\right\rangle\left(1 + \tanh\left(2 - 12\frac{c_w\Delta t}{h^2}\right)\right) \tag{13}$$

$$c_w = k_f(K + 4G/3) \tag{14}$$

where Δt is the current length of time step, k_f the permeability coefficient, K and G the bulk and shear modulus of solid skeleton respectively. h is a characteristic length of spatial discretization which is evaluated by $h = \sqrt{A_k^s}$ for each smoothing domain Ω_k^s, where A_k^s is the area of smoothing domain Ω_k^s shown in Fig. 1. As the time step and permeability grow from extremely low to a high level, the ε_f will decrease to zero gradually. In this way, the PPP can automatically guarantee accuracy and stability from undrained limit to drained condition (Choo and Borja, 2015; Zhang et al., 2022a, 2022b; Zhao and Borja, 2021).

2.3. Node-based gradient smoothing and integration stabilization

The node-based strain smoothing technique is introduced to improve the performance of FEM with low-order element (Liu et al., 2009a, 2009b), which originates from the stabilized conforming nodal integration in meshfree methods (Chen et al., 2001). In this approach, the gradient of shape function around a node is smoothed by taking the weighted average over a constructed smoothing domain intersected

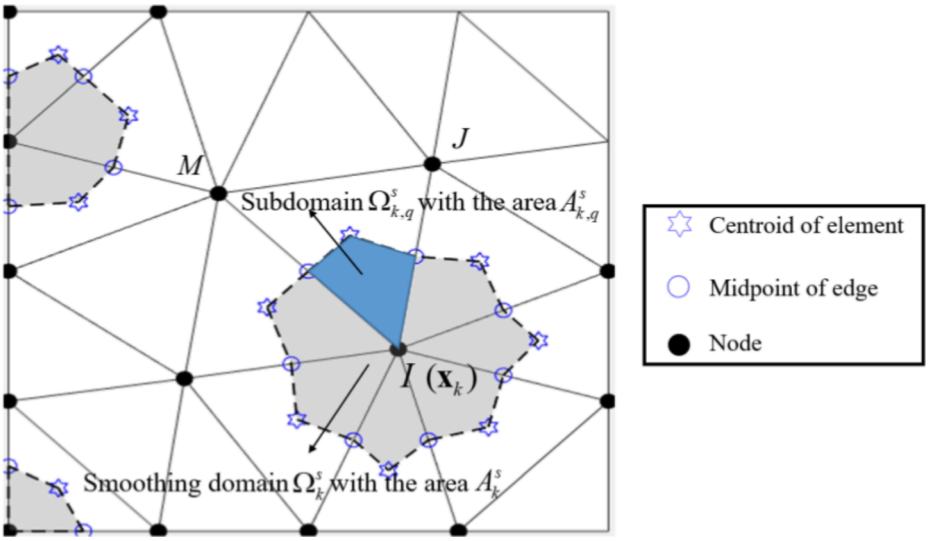

Fig. 1. Node-based smoothing domain and subdomain on the triangular mesh.

with several elements. Each smoothing domain works with the information propagated from all the connected elements, which makes NS-FEM more robust with mesh distortion and better accuracy in strain energy norm than FEM-T3 (Nguyen-Xuan and Liu, 2013; Wang et al., 2022a; Zeng and Liu, 2018). NS-FEM can reduce the volumetric locking of T3 element due to its "overly soft" property, but also bring numerical instability (Li and Liu, 2019; Nguyen-Xuan and Liu, 2013).

The first step from FEM-T3 to the node-based smoothed FEM is to construct the smoothing domains and subdomains as shown in Fig. 1. Regarding that all the vertices of these node-based domains are the centroids of elements or the midpoints of edges, this procedure is automatic with a given T3 mesh. Then the node-based gradient smoothing operator $\overline{\nabla}$ is defined in Eq. (15), with which the smoothed displacement gradient $\overline{\boldsymbol{B}}_u$ and fluid pressure gradient $\overline{\boldsymbol{B}}_p$ can be calculated as in Eqs. (16)–(17). This procedure can also be equivalently conducted in a contour integration approach, where only the evaluation of shape function is needed (Liu and Trung, 2016).(See Fig. 2)

$$\overline{\nabla} N_I(\boldsymbol{x}) = \int_{\Omega^s_k} \nabla N_I(\boldsymbol{x}) W(\boldsymbol{x}_I - \boldsymbol{x}) d\boldsymbol{x},$$
$$\text{with } W(\boldsymbol{x}_I - \boldsymbol{x}) = \begin{cases} 1/A^s_k, \boldsymbol{x} \in \overline{\Omega}^s_k \\ 0, \boldsymbol{x} \notin \overline{\Omega}^s_k \end{cases} \tag{15}$$

$$\overline{\boldsymbol{B}}_{u,I}(\boldsymbol{x}) = \int_{\Omega^s_k} \boldsymbol{B}_{u,I}(\boldsymbol{x}) W(\boldsymbol{x}_I - \boldsymbol{x}) d\boldsymbol{x} = \frac{1}{A^s_k} \sum_{q=1}^{n_k} A^s_{k,q} \boldsymbol{B}_{u,I(q)}, \ \forall \boldsymbol{x} \in \overline{\Omega}^s_k \tag{16}$$

$$\overline{\boldsymbol{B}}_{p,I}(\boldsymbol{x}) = \int_{\Omega^s_k} \boldsymbol{B}_{p,I}(\boldsymbol{x}) W(\boldsymbol{x}_I - \boldsymbol{x}) d\boldsymbol{x} = \frac{1}{A^s_k} \sum_{q=1}^{n_k} A^s_{k,q} \boldsymbol{B}_{p,I(q)}, \ \forall \boldsymbol{x} \in \overline{\Omega}^s_k \tag{17}$$

The spurious non-zero energy mode of NS-PFEM in the implicit dynamic scheme can be observed in the example of Section 3.4. The subdomain-based stress point stabilization is developed in this paper to efficiently treat this instability (Wang et al., 2022a; Wang et al., 2022b; Zhang et al., 2022a, 2022b). This idea originates from the modified stable nodal integration (SNI) method proposed by Chen and co-workers (Hillman and Chen, 2016; Puso et al., 2008; Wei et al., 2016). It uses the difference between the smoothed $\overline{\boldsymbol{B}}$ and the subdomain-smoothed $\overline{\boldsymbol{B}}^{sub}$ matrix to augment the smoothed stiffness and permeability matrices. In the T3 interpolation scheme, the subdomain-smoothed gradient $\overline{\boldsymbol{B}}^{sub}$ is just equal to the compatible gradient $\mathbf{B}$. The stabilized weak forms $\overline{\mathscr{I}}^h_u$ and $\overline{\mathscr{I}}^h_{p,stab}$ are presented in Eqs. (18)–(19), where $\Delta \boldsymbol{U}$ and $\Delta \boldsymbol{P}$ are the incremental nodal variables in the current load step. The derived stabilized node-based smoothed stiffness matrix $\overline{\boldsymbol{K}}_{uu}$, permeability matrix $\overline{\boldsymbol{K}}_{pp}$, coupling matrix $\overline{\boldsymbol{K}}_{up}$, and damping matrix $\overline{\boldsymbol{C}}$ are exhibited in Eqs. (20)–(23), where the subscript I and J denotes two nodes, and the global matrices are assembled by each smoothing domain. The numerical integration of Eqs. (20)–(23) can be simply performed by the 1-order Gaussian quadrature, that is, the multiplication of function value with its supporting area, because all the smoothed variables are constant on each subdomain. Besides, all the calculated variables are also constant on each node-based smoothing domain, so that the variables transferring between the nodes and quadrature points can be avoided in SNS-PFEM, which is more efficient than the traditional FEM.

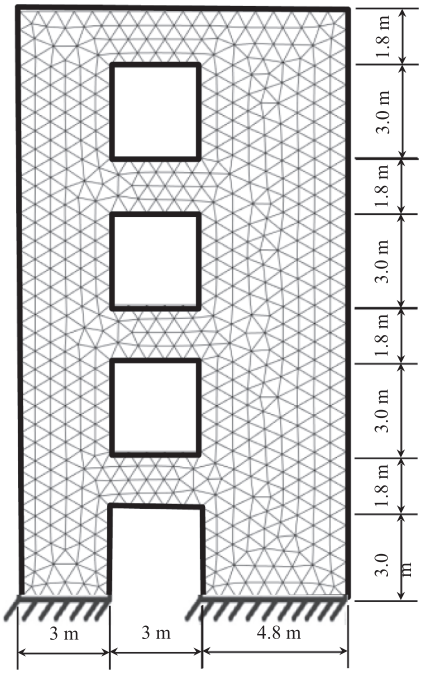

Fig. 2. Geometry and mesh of the shear wall with openings.

$$\overline{\mathscr{I}}_u^h = \boldsymbol{M}\ddot{\boldsymbol{U}} + \overline{\boldsymbol{C}}\dot{\boldsymbol{U}} + \int_\Omega \overline{\boldsymbol{B}}_u^T \overline{\boldsymbol{\sigma}} d\Omega + \left(\varepsilon_s \int_\Omega (\overline{\boldsymbol{B}}_u - \boldsymbol{B}_u)^T \boldsymbol{D}(\overline{\boldsymbol{B}}_u - \boldsymbol{B}_u) d\Omega\right)\Delta \boldsymbol{U} - \left(\int_\Omega \overline{\boldsymbol{B}}_u^T \boldsymbol{m}\boldsymbol{N}^p d\Omega\right)\boldsymbol{P} - \boldsymbol{F}^{ext} = 0 \tag{18}$$

$$\overline{\mathscr{I}}_{p,stab}^h = \left(\int_\Omega \overline{\boldsymbol{B}}_u^T \boldsymbol{m}\boldsymbol{N}_p d\Omega\right)^T \dot{\boldsymbol{U}} + \left(\int_\Omega \overline{\boldsymbol{B}}_p^T \boldsymbol{k}_f \overline{\boldsymbol{B}}_p d\Omega\right)\boldsymbol{P} + \left(\varepsilon_s \int_\Omega (\overline{\boldsymbol{B}}_p - \boldsymbol{B}_p)^T \boldsymbol{k}_f (\overline{\boldsymbol{B}}_p - \boldsymbol{B}_p) d\Omega\right)\Delta \boldsymbol{P} + \boldsymbol{S}\dot{\boldsymbol{P}} - \boldsymbol{Q}^{ext} = 0 \tag{19}$$

$$\left[\overline{\boldsymbol{K}}_{uu,IJ}\right]_{\Omega_k^s} = \int_{\Omega_k^s} \overline{\boldsymbol{B}}_{u,I}^T \boldsymbol{D} \overline{\boldsymbol{B}}_{u,J} d\boldsymbol{x} + \varepsilon_s \sum_{q=1}^{n_k} \int_{\Omega_{k,q}^s} (\overline{\boldsymbol{B}}_{u,I} - \boldsymbol{B}_{u,I})^T \boldsymbol{D}(\overline{\boldsymbol{B}}_{u,J} - \boldsymbol{B}_{u,J}) d\boldsymbol{x}$$
$$= \overline{\boldsymbol{B}}_{u,I}^T|_{\Omega_k^s} \boldsymbol{D} \overline{\boldsymbol{B}}_{u,J}|_{\Omega_k^s} A_k^s + \varepsilon_s \sum_{q=1}^{n_k} (\overline{\boldsymbol{B}}_{u,I}|_{\Omega_{k,q}^s} - \boldsymbol{B}_{u,I}|_{\Omega_{k,q}^s})^T \boldsymbol{D}(\overline{\boldsymbol{B}}_{u,J}|_{\Omega_{k,q}^s} - \boldsymbol{B}_{u,J}|_{\Omega_{k,q}^s}) A_{k,q}^s \tag{20}$$

$$\left[\overline{\boldsymbol{K}}_{pp,IJ}\right]_{\Omega_k^s} = \int_{\Omega_k^s} \overline{\boldsymbol{B}}_{p,I}^T \boldsymbol{k}_f \overline{\boldsymbol{B}}_{p,J} d\boldsymbol{x} + \varepsilon_s \sum_{q=1}^{n_k} \int_{\Omega_{k,q}^s} (\overline{\boldsymbol{B}}_{p,I} - \boldsymbol{B}_{p,I})^T \boldsymbol{k}_f (\overline{\boldsymbol{B}}_{p,J} - \boldsymbol{B}_{p,J}) d\boldsymbol{x}$$
$$= \overline{\boldsymbol{B}}_{p,I}^T|_{\Omega_k^s} \boldsymbol{k}_f \overline{\boldsymbol{B}}_{p,J}|_{\Omega_k^s} A_k^s + \varepsilon_s \sum_{q=1}^{n_k} (\overline{\boldsymbol{B}}_{p,I}|_{\Omega_{k,q}^s} - \boldsymbol{B}_{p,I}|_{\Omega_{k,q}^s})^T \boldsymbol{k}_f (\overline{\boldsymbol{B}}_{p,J}|_{\Omega_{k,q}^s} - \boldsymbol{B}_{p,J}|_{\Omega_{k,q}^s}) A_{k,q}^s \tag{21}$$

$$\left[\overline{\boldsymbol{K}}_{up,IJ}\right]_{\Omega_k^s} = \int_{\Omega_k^s} \overline{\boldsymbol{B}}_{u,I}^T \boldsymbol{m}\boldsymbol{N}_{p,J} d\boldsymbol{x} \tag{22}$$

$$\overline{\boldsymbol{C}} = a_1 \boldsymbol{M} + a_2 \overline{\boldsymbol{K}}_{uu} \tag{23}$$

By implementing SNI into NS-PFEM, a novel framework called stable node-based smoothed PFEM (SNS-PFEM) is achieved. It should be noted that the SNS-PFEM has lost the overly soft property and may suffer from volumetric locking when modelling nearly incompressible solids (Wang et al., 2022b). This difficulty can be alleviated through two approaches. First, the stabilization coefficient ε_s is used as a tuning parameter between 0 and 1. The value is usually fixed as 1, but can also be lowered to release some softening so long as the stabilization is guaranteed (Moutsanidis et al., 2020; Puso et al., 2008). Second, a novel locking-free SNS-PFEM with selective integration and bubble function has been proposed and fully validated (Wang et al., 2022b). It is efficient in dealing with volumetric locking but requires additional computational costs. This paper focuses on hydromechanical modelling with compressible soil skeleton, and Poisson's ratio is set smaller than 0.4 in all the simulations.

2.4. Temporal integration with the CH generalized-α method

From the view of mathematics, the SNS-FEM equations of hydro-mechanical coupled dynamics are a group of second-order differential equations about displacement and pore pressure. The dynamic responses should be acquired by step-by-step direct temporal integration, especially for the highly nonlinear geotechnical problems since the modal and frequency analysis are unfeasible. For the implementation of temporal integration, the time range is first divided into a lot of intervals, and then some assumptions of the variation of state variables in one-time interval are introduced to calculate the difference from old current t_n to new current t_{n+1}. The explicit integration methods are popular for their low computational cost, but the stability condition will require high permeability and small time step in the hydro-mechanical coupled analysis (Jin and Yin, 2022; Soga et al., 2016; Xu et al., 2017a). On the contrary, many implicit schemes are unconditionally stable and error controllable under adequate parameter values, which is more suitable for long-term, highly nonlinear geotechnical problems.

Numerous implicit time marching schemes have been applied in geotechnical dynamic problems, such as the Wilson-θ method (White and Borja, 2008), Newmark-β method (Newmark, 1965), WBZ-α method (Wood et al., 1980), HHT-α method (Hilber et al., 1977), CH generalized-α method (Han et al., 2015; Sabetamal et al., 2014), to name a few. The CH generalized-α method proposed by Chung and Hulbert is superior because it can preserve the numerical damping of high frequencies and second-order accuracy of low frequencies simultaneously (Han et al., 2015; Sabetamal et al., 2014). The fundamental idea is that the different state variables are evaluated at different instances with separate weights in an average form. As shown in Eq. (24), the acceleration in the inertia term is evaluated at $t_{n+1-\alpha_m}$ with weights α_m and $1-\alpha_m$, while the velocity, displacement, pore pressure, load and flow flux terms are controlled by another coefficient α_f.

$$\begin{cases} \ddot{\boldsymbol{U}}_{t_{n+1-\alpha_m}} = \alpha_m \ddot{\boldsymbol{U}}_{t_n} + (1-\alpha_m)\ddot{\boldsymbol{U}}_{t_{n+1}} \\ \dot{\boldsymbol{U}}_{t_{n+1-\alpha_f}} = \alpha_f \dot{\boldsymbol{U}}_{t_n} + (1-\alpha_f)\dot{\boldsymbol{U}}_{t_{n+1}} \\ \boldsymbol{U}_{t_{n+1-\alpha_f}} = \alpha_f \boldsymbol{U}_{t_n} + (1-\alpha_f)\boldsymbol{U}_{t_{n+1}} \\ \boldsymbol{P}_{t_{n+1-\alpha_f}} = \alpha_f \boldsymbol{P}_{t_n} + (1-\alpha_f)\boldsymbol{P}_{t_{n+1}} \\ \boldsymbol{F}^{ext}_{t_{n+1-\alpha_f}} = \alpha_f \boldsymbol{F}^{ext}_{t_n} + (1-\alpha_f)\boldsymbol{F}^{ext}_{t_{n+1}} \\ \boldsymbol{Q}^{ext}_{t_{n+1-\alpha_f}} = \alpha_f \boldsymbol{Q}^{ext}_{t_n} + (1-\alpha_f)\boldsymbol{Q}^{ext}_{t_{n+1}} \end{cases} \tag{24}$$

The displacement and velocity are approximated using the Newmark-β method with two controlling parameters β and γ in Eq. (25). The temporal integration of pore pressure is conducted using the Wilson-θ method in Eq. (25). These approximations are based on the theories of the truncated Taylor's expansions and mean value theorem. Therefore, the integration parameters control the accuracy and stability of the numerical solutions.

$$\begin{cases} \dot{\boldsymbol{U}}_{t_{n+1}} = \dot{\boldsymbol{U}}_{t_n} + ((1-\gamma)\ddot{\boldsymbol{U}}_{t_n} + \gamma\ddot{\boldsymbol{U}}_{t_{n+1}})\Delta t \\ \boldsymbol{U}_{t_{n+1}} = \boldsymbol{U}_{t_n} + \dot{\boldsymbol{U}}_{t_n}\Delta t + ((\frac{1}{2}-\beta)\ddot{\boldsymbol{U}}_{t_n} + \beta\ddot{\boldsymbol{U}}_{t_{n+1}})\Delta t^2 \\ \int_{t_n}^{t_{n+1}} \boldsymbol{P} dt = \boldsymbol{P}_{t_{n+\theta}}\Delta t = ((1-\theta)\boldsymbol{P}_{t_n} + \theta \boldsymbol{P}_{t_{n+1}})\Delta t \end{cases} \tag{25}$$

The time-discrete algebraic equations to be solved are exhibited in Eq. (26). Different treatments are applied to the momentum and mass conservation equations respectively. The equilibrium weak form in Eq. (18) is evaluated at different instances for the inertia term (at $t_{n+1-\alpha_m}$) and the remaining terms (at $t_{n+1-\alpha_f}$). The mass conservation equation (19) is integrated at the time interval from t_n to t_{n+1}. In the aforementioned numerical framework, the unconditional stability and second-order accuracy of the CH generalized-α method, Newmark-β method and Wilson-θ method can be achieved only when the inequality constraints Eq. (27) are satisfied, which have been proved in Han et al (Han et al., 2015). In this study, all the time integration parameters are fixed to meet the requirements as follows: $\alpha_f = 0.45$, $\alpha_m = 0.35$, $\beta = 0.3$, $\gamma = 0.6$, $\theta = 1$.

$$\begin{cases} \boldsymbol{M}\ddot{\boldsymbol{U}}_{t_{n+1-\alpha_m}} + \overline{\boldsymbol{C}}\dot{\boldsymbol{U}}_{t_{n+1-\alpha_f}} + \overline{\boldsymbol{F}}^{ints}(\boldsymbol{U}_{t_{n+1-\alpha_f}}) - \overline{\boldsymbol{K}}_{up}\boldsymbol{P}_{t_{n+1-\alpha_f}} = \boldsymbol{F}^{ext}_{t_{n+1-\alpha_f}} \\ \overline{\boldsymbol{K}}_{up}^T(\boldsymbol{U}_{t_{n+1}} - \boldsymbol{U}_{t_n}) + \overline{\boldsymbol{K}}_{pp}\int_{t_n}^{t_{n+1}} \boldsymbol{P} dt + \boldsymbol{S}\int_{t_n}^{t_{n+1}} \dot{\boldsymbol{P}} dt = \int_{t_n}^{t_{n+1}} \boldsymbol{Q}^{ext} dt \end{cases} \tag{26}$$

$$\begin{cases} \alpha_m \leqslant \alpha_f \leqslant 0.5 \\ \beta \geqslant \dfrac{1+2(\alpha_f - \alpha_m)}{4} \\ \gamma = 0.5 - \alpha_m + \alpha_f \\ \theta > 0.5 \end{cases} \tag{27}$$

The nonlinear Eqs. (26) can be solved using the standard Newton-Raphson iteration procedure. The *i*th iteration in the time step t_{n+1} is exhibited in Eq. (28), where the equivalent stiffness matrix is defined in

Eq. (29). The detailed algebraic derivations are presented in Appendix B. Noticing that we can also simulate the dynamics of single solid phase by only using the solid-related subblocks in Eq. (28).

$$\begin{bmatrix} \widehat{\boldsymbol{K}}_{uu} & -(1-\alpha_f)\overline{\boldsymbol{K}}_{up} \\ -(1-\alpha_f)\overline{\boldsymbol{K}}_{up}^T & -(1-\alpha_f)\left(\theta\Delta t\overline{\boldsymbol{K}}_{pp}+\boldsymbol{S}\right) \end{bmatrix}_{t_{n+1}} \begin{bmatrix} \delta\boldsymbol{U} \\ \delta\boldsymbol{P} \end{bmatrix}_{t_{n+1}}^{(i)} = \begin{bmatrix} \Delta\boldsymbol{R}_u \\ \Delta\boldsymbol{R}_p \end{bmatrix}_{t_{n+1}}^{(i)} \tag{28}$$

$$\widehat{\boldsymbol{K}}_{uu} = \frac{1-\alpha_m}{\beta\Delta t^2}\boldsymbol{M}+\frac{(1-\alpha_f)\gamma}{\beta\Delta t}\overline{\boldsymbol{C}}+(1-\alpha_f)\overline{\boldsymbol{K}}_{uu} \tag{29}$$

2.5. Remeshing strategies

The large deformation process can be adequately simulated with the remeshing strategy and variable mapping in the traditional particle finite element framework. For the SNS-PFEM, however, only the remeshing procedure is needed, because all the key variables are carried directly by the node-based smoothing domains. In each analysis step with relatively small deformation, the calculation is conducted using the standard SNS-FEM, which is similar to some studies in the PFEM-based or SPFEM-based geotechnical simulations (Jin et al., 2020a, 2020b; Zhang et al., 2020; Zhang et al., 2016a, 2016b). Then the position of nodes (particles) is updated using incremental displacement. Next, a new mesh will be established with the remeshing methods, namely the Delaunay triangulation and α-shape method (Cremonesi et al., 2020), where the node connectivity may have been changed because the principles behind the Delaunay triangulation can automatically avoid the mesh distortion. Finally, the next analysis step is carried out based on the updated state variables and mesh.

The α-shape method is likely to incur some volume fluctuation in the calculation domain, and then the principle of mass conversation may be violated. As reported in the previous study on PFEM (Zhang et al., 2013), this error can be controlled by adjusting the parameter α for each specific problem to improve the accuracy of the boundary identification, and the range $1.1\leqslant\alpha\leqslant1.6$ is recommended. The volume fluctuation can be reduced to lower than 6 % for the soil collapse problem (Zhang et al., 2013) and around 1 % for the water dam break simulation (Franci and Cremonesi, 2017). Besides, for the problems with partly predictable boundary evolution, the geometrically constrained Delaunay triangulation could be used (Cremonesi et al., 2020). This approach can also improve the accuracy of boundary identification and further reduce the error in mass fluctuation.

Noticing that the advanced remeshing techniques, such as adding or removing nodes, Laplacian smoothing of node distribution and adaptive mesh refinement, have not been applied here. If extremely large deformation (i.e., exploding or granular flowing) is taken place and some nodes become too close or distinct from others, the remeshing strategy used in this paper is not sufficient to handle such problems. The aforementioned mesh refinement techniques should be considered (Carbonell et al., 2022; Moutsanidis et al., 2020).

The dynamic SNS-PFEM is implemented within a self-developed MATLAB code suite including the modules of pre-processing, solver and post-processing, which is developed based on our previous studies (Wang et al., 2022a; Wang et al., 2022b). The computational cycle of the SNS-PFEM for hydro-mechanical coupled dynamics is summarized as follows.

1. *Initialize the geometry and all the given parameters.*
2. *Discretize the domain into a cloud of nodes (particles). Form the mesh using Delaunay triangulation.*
3. *Assemble the matrices including (lumped) mass, stabilized smoothed stiffness, permeability, hydro-mechanical coupling, PPP term and damping matrices. Apply all the essential boundary conditions.*
4. *Solve the nonlinear dynamic SNS-FEM equations in a single step using the Newton-Raphson iteration scheme until the convergence criterion is satisfied.*
5. *Update the positions of nodes and renew all the physical quantities of interest.*
6. *Rebuild the mesh with Delaunay triangulation and α-shape method. Then go back to step 3 until all the calculation steps are finished.*

3. Validation

In this section, several examples are presented to verify the numerical accuracy and stability of the proposed SNS-PFEM, highlighting the performance of the nodal integration and pore pressure stabilization techniques. The first two problems, i.e., the free vibration of a shear wall and the dynamic response of an elastoplastic beam under a sudden load, only concern the solid phase without water. While the remaining three examples investigate the dynamic effects of hydro-mechanical coupling with 1D and 2D geometry in small and large deformation conditions. Both linear elastic and elastoplastic materials are taken into consideration.

3.1. Free vibration analysis of a shear wall

In this example, the free vibration analysis of an elastic shear wall with four openings is conducted. The plane stress problem is set with a uniform T3 mesh of 646 nodes and 1126 elements. The material parameters are set as Young's modulus $E = 1$ kPa, Poisson's ratio $\nu = 0.2$, and density $\rho = 0.1$ kg/m^3, just the same as the values adopted by the meshless local Petrov-Galerkin method (MLPG) (Gu and Liu, 2001), boundary element method (BEM) (Brebbia, 1984) and edge-based smoothed FEM (ES-FEM) (Liu et al., 2009a, 2009b). The standard eigenvalue and eigenvector analysis is performed using Eq. (30), where the NS-PFEM is implemented by reducing the integration stabilization coefficient ε_s to 0.

$$\overline{\boldsymbol{K}}_{uu}\boldsymbol{\Phi}-\omega^2\boldsymbol{M}\boldsymbol{\Phi}=\boldsymbol{0} \tag{30}$$

Table. 1 presents the first eight natural frequencies acquired by different numerical methods. It shows that the frequencies of SNS-PFEM are quite close to the reference solutions, and fall into the intervals between FEM-T3 and FEM-T6. However, the frequencies of NS-PFEM are significantly lower than that of the remaining methods, which indicates the typical "overly soft" property. Fig. 3 presents the corresponding first eight vibration modes. All the patterns by different methods are similar to each other, except some of the high-frequency modes of NS-PFEM highlighted by the red arrows exhibit weird sawtooth noises. This is due to the spurious non-zero energy mode of direct nodal integration, which can be effectively cured by the integration stabilization of SNS-PFEM. The foregoing results demonstrate that the SNS-PFEM is accurate in the free vibration analysis and effective in circumventing the overly soft property and spurious modes of NS-PFEM.

3.2. Deep elastoplastic beam under suddenly applied loading

The second example investigates the dynamic response of a deep beam under the suddenly applied loading to verify the correctness of the time integration algorithm, especially concerning material nonlinearity. As shown in Fig. 4, a half geometry with 431 nodes and 764 elements is taken due to symmetry. The modelling parameters are set as the same in the reference paper using BEM (Pavlatos and Beskos, 1994): L = 24 m, H = 6 m, Young's modulus $E = 100$ kPa, Poisson's ratio $\nu = 0.333$, and the density $\rho = 1500$ kg/m^3. The von Mises elastoplastic model with the yield stress $\sigma_y = 0.16$ kPa is used, and the suddenly applied pressure $\bar{p} = 0.015$ kPa is applied, which equals the collapse load in the plane stress condition. The time step is fixed as $\Delta t = 0.5$ s.

The Fig. 5 (a, b) and (c, d) depict the time history of the vertical

Table 1
Natural frequencies of a shear wall (rad/s).

Mode	MLPG (Ref)	BEM (Ref)	FEM-T3	FEM-T6	NS-PFEM	**SNS-PFEM**
1	2.069	2.079	2.105782	2.031193	1.879306	**2.092357**
2	7.154	7.181	7.194403	6.998749	6.643763	**7.163196**
3	7.742	7.644	7.638199	7.608918	7.523335	**7.633736**
4	12.163	11.833	12.2289	11.6241	10.57635	**12.11086**
5	15.587	15.947	15.66034	15.09706	14.13232	**15.57323**
6	18.731	18.644	18.56965	18.15624	17.08996	**18.5096**
7	20.573	20.268	20.15568	19.67854	18.54825	**20.0879**
8	23.081	22.765	22.5063	21.99649	20.71811	**22.43498**

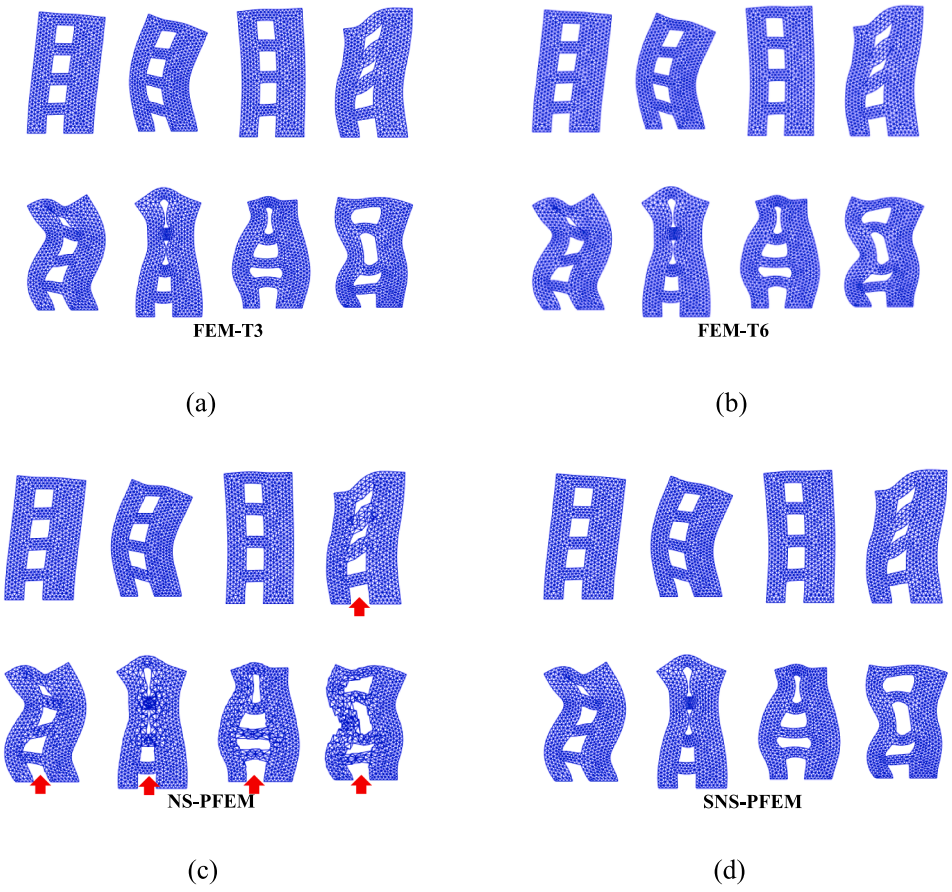

Fig. 3. First eight vibration modes of the shear wall with different methods.

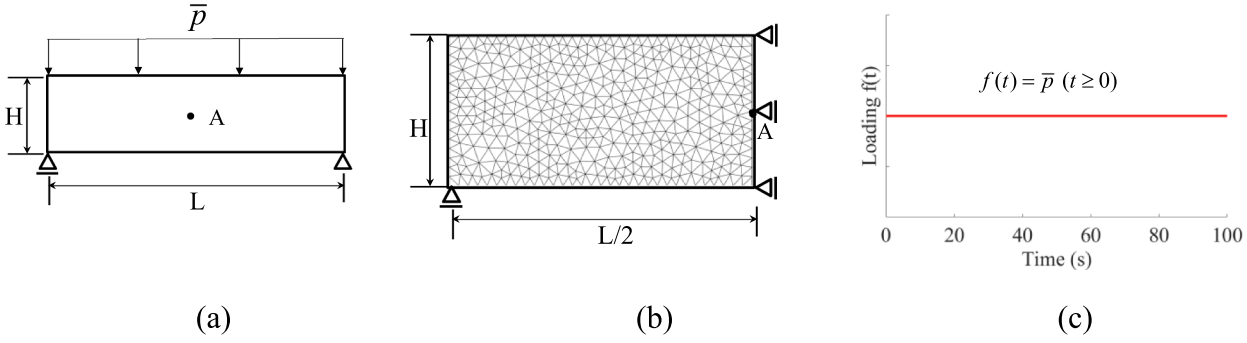

Fig. 4. Simply supported beam: (a) geometry and boundary conditions; (b) mesh with half geometry; (c) suddenly applied load.

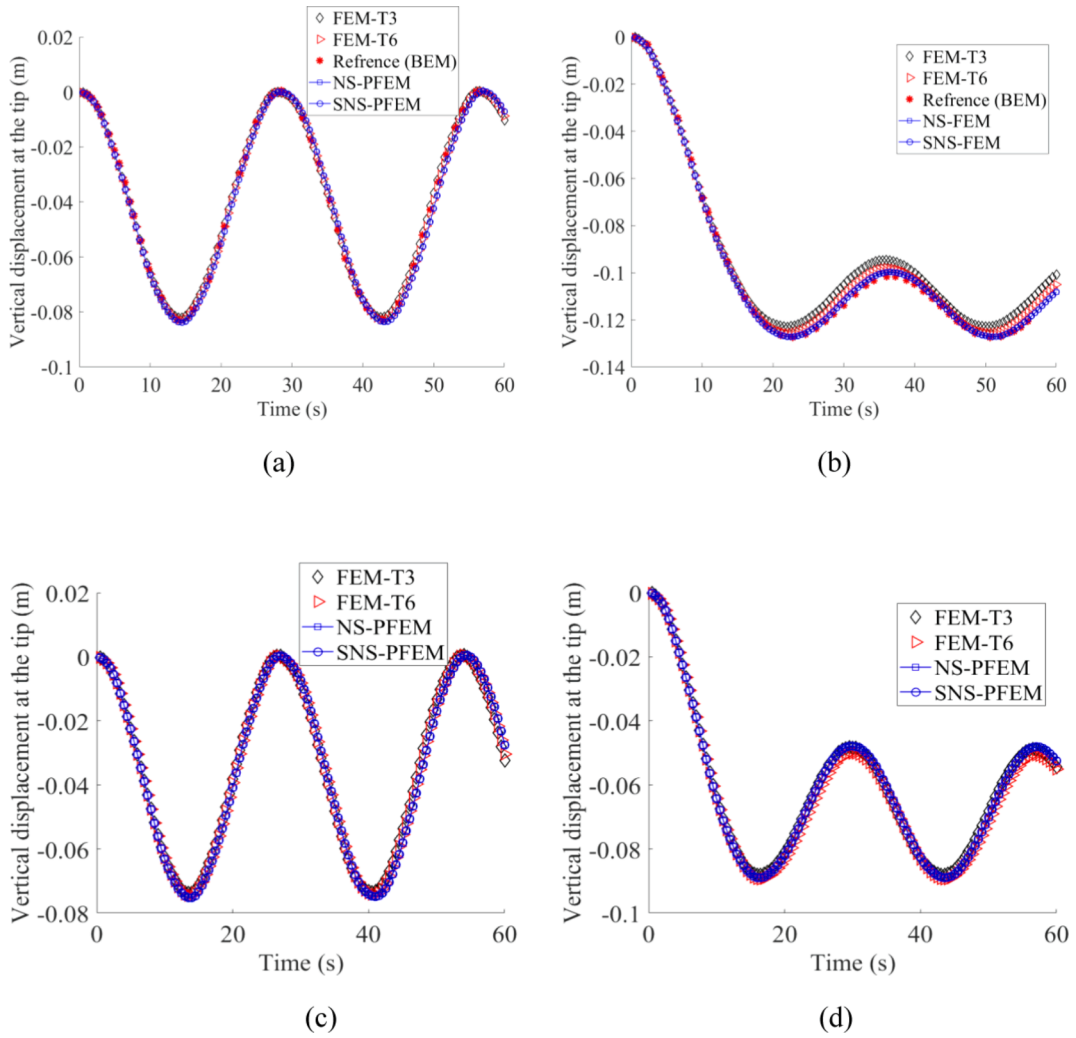

Fig. 5. Vertical displacement history of point A: (a) elastic plane stress; (b) elastoplastic plane stress; (c)elastic plane strain; (d) elastoplastic plane strain.

displacement at point A in the plane stress and plane strain conditions respectively. For the elastic cases, the beam vibrates in a perfectly harmonic way. While for the elastoplastic cases, the beam first undergoes a large displacement including some plastic deformation and then vibrates in the range of small elastic deformation. The results of SNS-PFEM and NS-PFEM agree well with those of the FEM and BEM in both plane strain and plane stress conditions. It reveals that the CH generalized-α method can give accurate dynamic responses in SNS-PFEM with both linear and nonlinear materials. Besides, the necessity of nodal integration stabilization is not obvious in this simple case.

3.3. Dynamic consolidation of saturated elastic column

The dynamic consolidation of a saturated elastic porous column is demonstrated in Fig. 6. The geometry is discretized into 312 nodes and 540 elements. The time-varying uniform pressure is applied on the drained top, which first rises straightly to 1 kPa in 0.02 s and then oscillates harmonically with the amplitude of 0.25 kPa. The material parameters are set as the same as reference (Han et al., 2015): Young's modulus $E = 10$ MPa, Poisson's ratio $\nu = 0.2$, and the density $\rho = 2000$ kg/m^3. In the first simulation of a drained condition, the time step takes the value of $\Delta t = 0.005$ s, and the permeability is set as $k = 0.01$ m/s. The polynomial pressure projection is activated in hydro-mechanical coupled analysis by default. The variation of the vertical displacement at surface point A and the pore pressure at bottom point B with different numerical methods are presented in Fig. 7. It shows the trend of settlement and pore pressure dissipation with some fluctuations due to the wave loading. The abbreviation T3/6 means the 6-node quadratic interpolation for displacement and 3-node linear interpolation for pore pressure, which is proved free from nonphysical pressure oscillations in FEM. The results indicate that both the NS-PFEM and SNS-PFEM with PPP can get accurate and stable solutions in the 1D dynamic consolidation case with high permeability.

To trigger the non-physical pore pressure oscillations, the second analysis is conducted to model a nearly undrained condition. The time step takes the value of $\Delta t = 0.001$ s, and the extremely low permeability is set as $k = 10^{-15}$ m/s. The time history of pore pressure at point B with different numerical treatments is exhibited in Fig. 8, and the contour of pore pressure at $t = 0.05$ s is shown in Fig. 9, where the stabilizations can be turned off by setting the coefficients ε_s and ε_f equals to 0. In Fig. 8 (a, c), the pore pressure experiences huge random oscillations when the PPP is not activated. Some slight instability can still be observed in the first 0.2 s with the NS-PFEM with PPP, as shown in Fig. 8 (b). The completely stable solution can be achieved only with the SNS-PFEM with PPP, as shown in Fig. 8 (d). From the contours of pore pressure in Fig. 9, a typical checkerboard pattern will appear when the PPP is not used, which indicates a similar distribution to the volumetric locking of nearly incompressible solids. In conclusion, the non-physical pore pressure oscillation is severe in the undrained limit of hydro-mechanical coupled dynamic analysis with SNS-PFEM, and it can be overcome by the PPP technique.

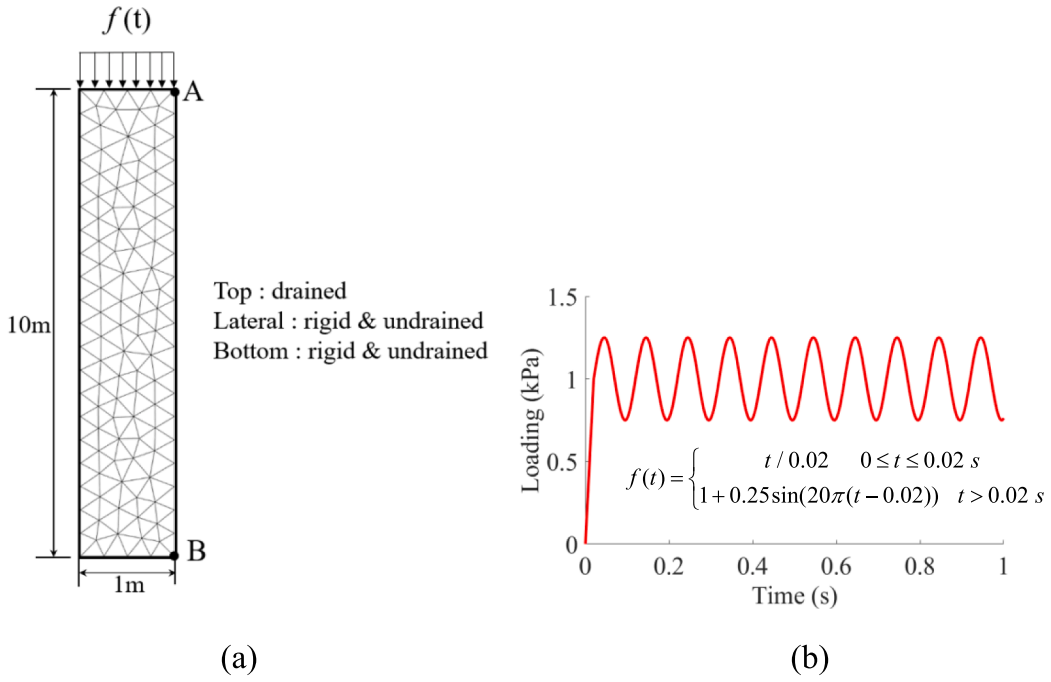

Fig. 6. 1D dynamic consolidation: (a) geometry and boundary conditions; (b) load history.

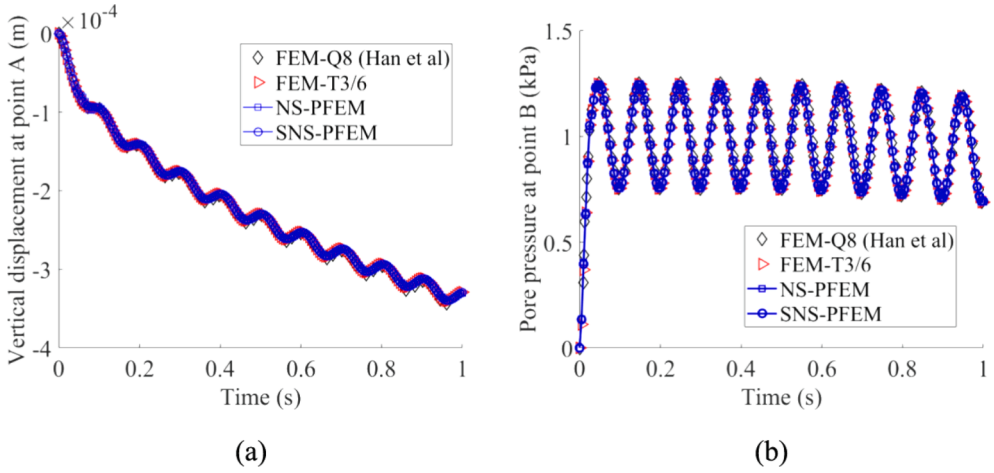

Fig. 7. Time histories for: (a) vertical displacement at point A; (b) pore pressure at point B.

3.4. 2D wave propagation

In this example, the dynamical wave propagation in a saturated rectangular region is studied to further investigate the performance of the proposed SNS-PFEM (Jin and Yin, 2022; Monforte et al., 2019; Wang et al., 2021a, 2021b). The plane strain condition is used with the following properties: Young's modulus $E = 14.5$ MPa, Poisson's ratio $\nu = 0.3$, the density $\rho = 2000$ kg/m^3, and the permeability $k = 0.01$ m/s. For the Drucker-Prager model used, the parameters are set as the friction angle $\phi = 5°$, dilatancy angle $\psi = 5°$, and cohesion $c = 15$ kPa. The impulse harmonic pressure of half period 0.04 s is uniformly applied on the 1 m width strip C to D, as shown in Fig. 10. The region is discretized with 1729 nodes and 3263 elements. The time step is set as $\Delta t = 0.001$ s. Two monitoring points are set to record the evolution of the displacement at point A and pore pressure at point B.

The results of the elastic case are exhibited in Fig. 11 and Fig. 13. The in-plane movement of surface point A presents a typical quasi-elliptic trajectory, which is generated by the propagation of elastic Rayleigh wave. The time history of pore pressure at interior point B in undergoes four-stage ups and downs due to the coupling effect of impulse force and inertia, and gradually dissipates at the final stage. The pore pressure with the wave fields (using a magnifying factor of 300) at different scenarios are presented in Fig. 13, which agrees quite well with the previous studies (Brezzi and Bathe, 1990; Kontoe et al., 2008; Sabetamal et al., 2016). In Fig. 11, the results of SNS-PFEM agree well with the references, while the displacement curve of NS-PFEM is different from the others at the final stage, and the pore pressure of NS-PFEM experiences non-physical oscillations at the dissipation stage. In Fig. 12, the simulations are performed with different mesh densities and time steps. All the results are stable, and the evolution of pore pressure is not influenced by the time step and spatial discretization. The displacements calculated with different time steps are close to each other for the same mesh, which indicates the generalized-α method is accurate, unconditionally stable and independent of time step. The maximum displacement of fine mesh is larger than that of the coarse mesh, showing the coarse mesh could give rigid response in the dynamic SNS-PFEM.

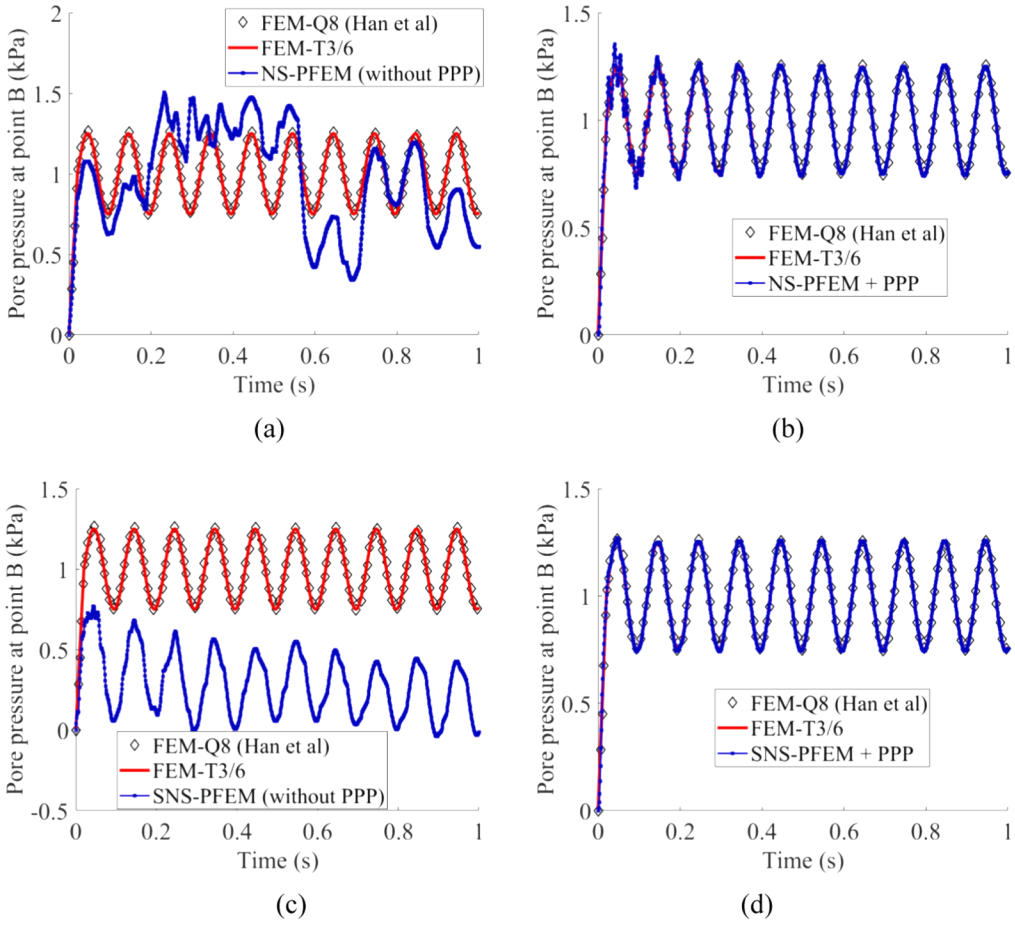

Fig. 8. Evolution of the pore pressure at point B under extremely low permeability with different numerical settings: (a) NS-PFEM without PPP; (b) NS-PFEM with PPP; (c) SNS-PFEM without PPP; (d) SNS-PFEM with PPP.

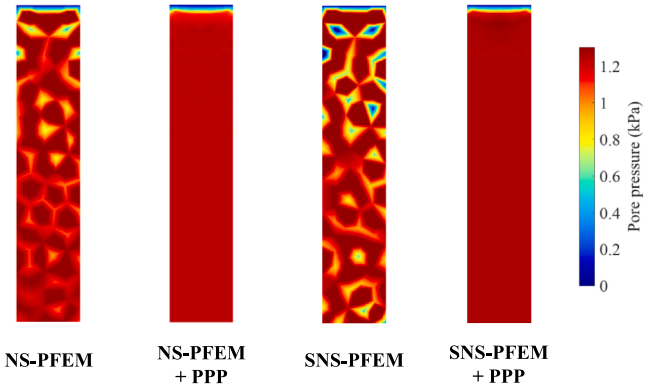

Fig. 9. Contour of the pore pressure under extremely low permeability with different numerical settings.

The results of the elastoplastic case are presented in Fig. 14 and Fig. 15. The displacement trajectory of surface point A is no longer quasi-elliptic but an unclosed curve with permanent plastic deformation. The pore pressure of point B also undergoes similar four stages, but its dissipation is quite slower. The pore pressure with rescaled wavefields at different times shows that a plastic concave is formed at the loading strip. Also, the results of SNS-PFEM are in good accordance with the FEM, while the results of NS-PFEM are not so reasonable. Fig. 16 visually illustrates the comparisons of the contours of pore pressure and shear stress of two different methods. The distributions acquired by the NS-PFEM undergo severe numerical noises, which is typical for the spurious non-zero energy modes, while the distributions by SNS-PFEM are quite smooth. It can be concluded that the proposed SNS-PFEM is stable and accurate in the 2D wave propagation problem. Besides, the nodal integration stabilization technique plays a decisive role in curing the severe instability of NS-PFEM in hydro-mechanical coupled dynamic problems.

3.5. *Strip footing penetration*

This example investigates the strip footing penetration into the saturated Mohr-Coulomb (MC) soil to further validate the performance of the dynamic SNS-PFEM involving large deformation. The same problem has been simulated in previous studies with ALE (Sabetamal et al., 2016) and MPM (Salgado and Bisht, 2021). The plane strain condition is used with the following soil properties: Young's modulus $E = 2$ MPa, Poisson's ratio $\nu = 0.3$, the density $\rho = 1000$ kg/m^3, permeability $k = 10^{-6}$ m/s, friction angle $\phi = 20°$, dilatancy angle $\psi = 0°$, and cohesion $c = 10$ kPa. All the soil properties are set as the same as the referenced studies for comparison (Sabetamal et al., 2016; Salgado and Bisht, 2021). The uniform vertical displacement of $U = -2.5$ m is applied over a period 1 s on the strip with width $B = 1$ m. The time step is set as $\Delta t = 0.01$ s. The half geometry is taken due to symmetry which is discretized with a locally refined mesh of 3545 nodes and 6890 elements, as shown in Fig. 17.

The contours of velocity and equivalent deviatoric plastic strain are exhibited in Fig. 18, which are quite smooth, indicating the correctness of the remeshing scheme. As Fig. 19 shows, the normalized soil

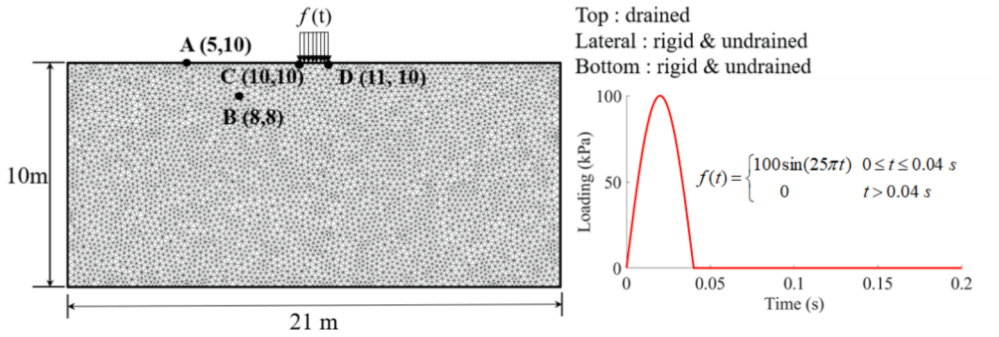

Fig. 10. Set-up for the 2D wave propagation in the rectangular domain.

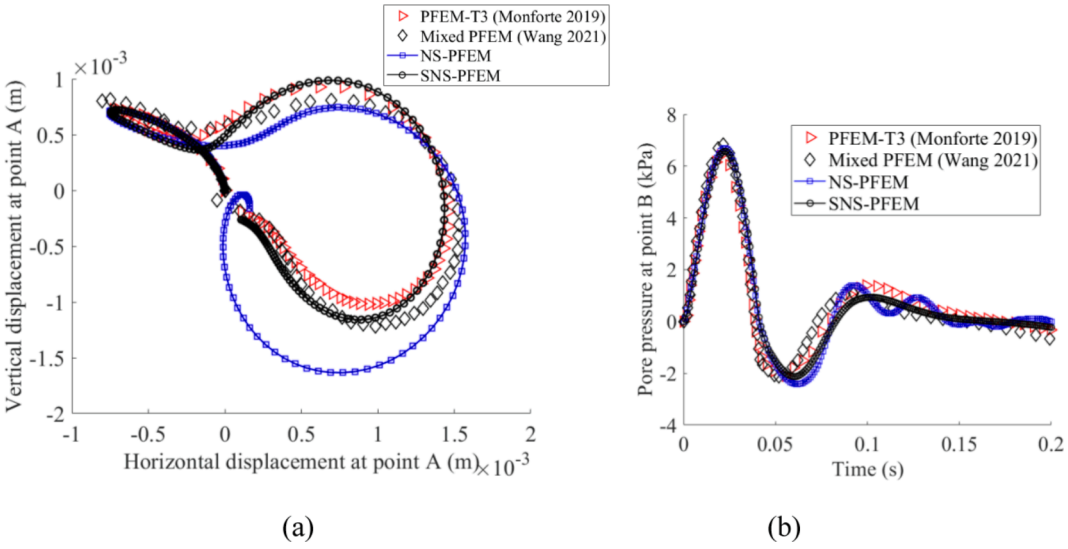

Fig. 11. (a) The motion of point A; (b) the evolution of pore pressure at point B for the elastic case.

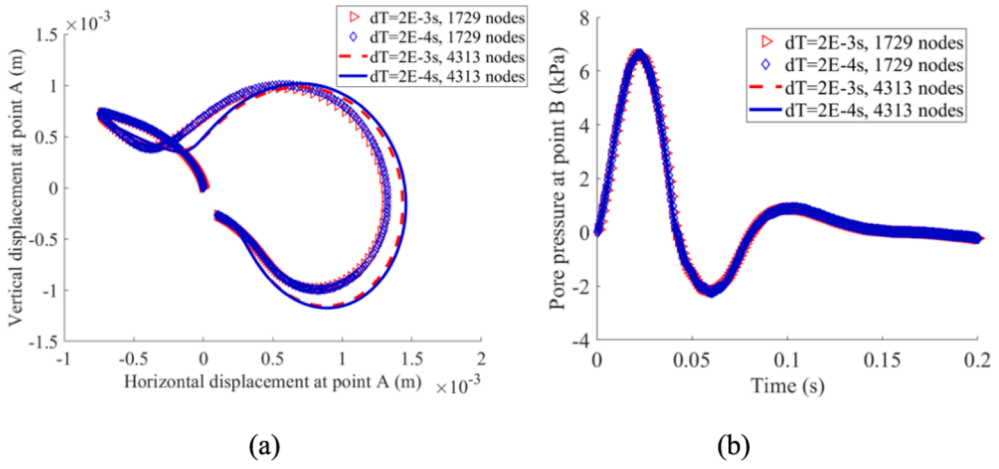

Fig. 12. (a) The motion of point A; (b) the evolution of pore pressure at point B with different mesh densities and time steps in SNS-PFEM.

resistance-displacement curve by the proposed coupled SNS-PFEM agrees well with the referenced solutions of ALE and MPM, even when the penetration goes deep. The jump of stiffness and mass in remeshing is believed to cause the slight fluctuation of the resistance-displacement curve with SNS-PFEM, which is unavoidable in PFEM-class methods (Jin et al., 2020a, 2020b; Monforte et al., 2017a, 2017b). Therefore, all the obtained results demonstrate the proposed SNS-PFEM performs well in simulating dynamic problems involving large deformation.

4. Applications

In this section, three examples of hydro-mechanical coupled dynamics are simulated to show the power of the proposed SNS-PFEM in modelling some sophisticated geotechnical problems. The first example investigates the dynamic response of the elastic porous seabed under the high-order wave and current loading. The second example simulates the whole process of the Selborne slope experiment from the failure

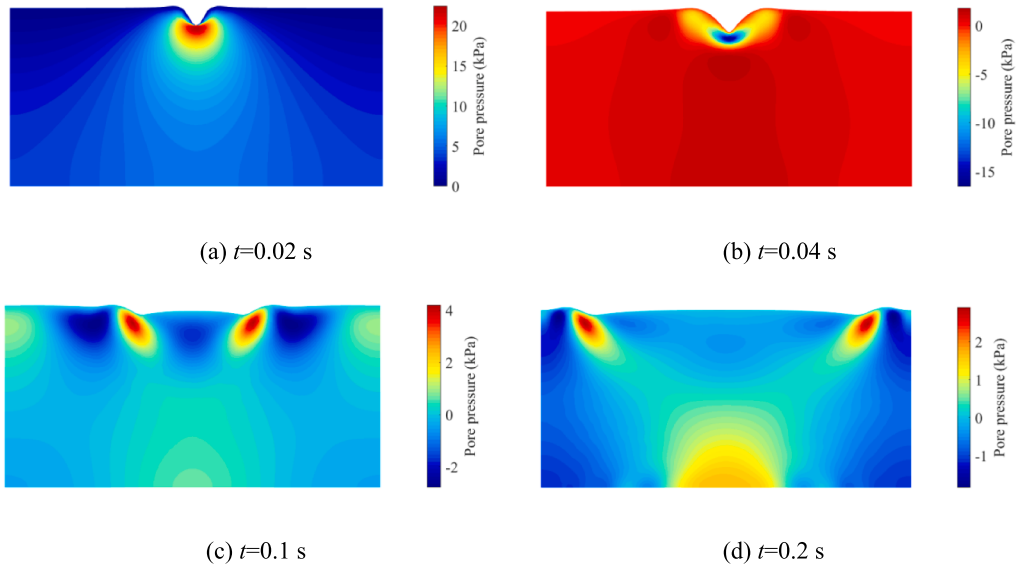

Fig. 13. Contour of the pore pressure with deformed configuration (scale factor 300) at different scenarios for the elastic case.

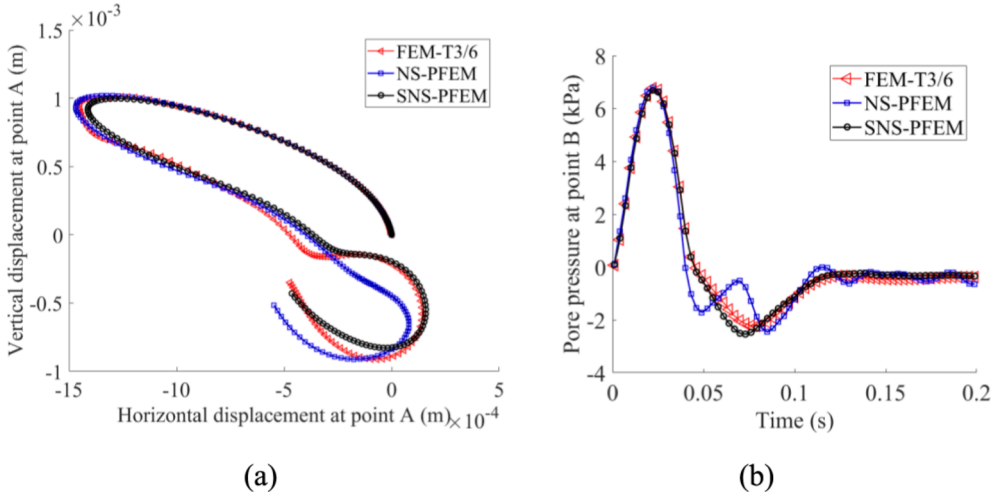

Fig. 14. (a) The motion of point A; (b) the evolution of pore pressure at point B for the elastoplastic case.

initiation to the post-failure movement. The last example explores the dynamic response of a saturated soil slope under a realistic seismic loading.

4.1. Seabed under wave and current loading

It has been widely validated by experiments and mathematical modelling that the ocean waves and currents will incur the transient dynamic response in the poroelastic seabed (De Groot et al., 2006; Ye and Jeng, 2012). As shown in Fig. 20, the wave with crests and troughs proceeds in one direction and exserts the periodic tension–compression dynamic pressure on the free drainage surface of the seabed. It tends to induce the alternate positive–negative distribution of dynamic pore pressure and dynamic effective stress (Monforte et al., 2017a, 2017b). When the dynamic excess pore pressure exceeds the initial static vertical effective stress, the soil will liquefy and lose its strength and stability. In this section, two types of wave loads are used for consistency with reference solutions. The formulations of the pressure of the second-order Stokes wave theory (Xu et al., 2017a) are presented in Eq. (31), and the pressure of the third-order nonlinear wave with a uniform current (Ye and Jeng, 2011; Ye and Jeng, 2012) are presented in Eqs. (32)–(33). The explanations for each variable are listed as follows: ρ is the density of the seawater, g the gravity acceleration, H the wave height, ω the wave angular frequency, λ the wave number, d the water depth, L the wavelength and U_0 the current velocity. A finite domain is adopted here to model the dynamic responses within a half-infinite field, which may cause some near-boundary error due to the wave flection. The computational domain is set as more than 3 times longer than the wavelength, together with the simply fixed and impervious lateral boundaries, which has been proved to preserve computational accuracy in the region, not near the boundary (Hughes, 2000; Monforte et al., 2017a, 2017b). If a smaller geometry is used, or the transient wave radiation in the porous domain needs to be investigated, more advanced treatments such as the artificial viscous-spring boundary should be considered (Xu et al., 2017b).

$$P_{b,2} = \frac{\rho g H}{2\cosh(\lambda d)}\cos(\lambda x - \omega t) + \frac{3\pi\rho g H^2}{8L}\frac{\tanh(\lambda d)}{\sinh^2(\lambda d)}\left[\frac{1}{\sinh^2(\lambda d)} - \frac{1}{3}\right]\cos 2(\lambda x - \omega t) \tag{31}$$

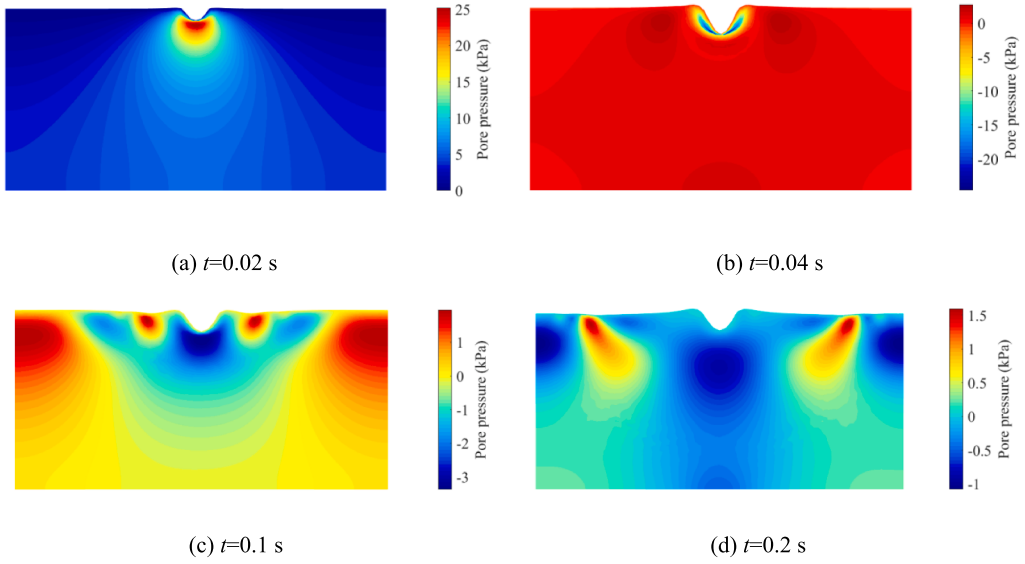

Fig. 15. Contour of the pore pressure with deformed configuration (scale factor 300) at different scenarios for the elastoplastic case.

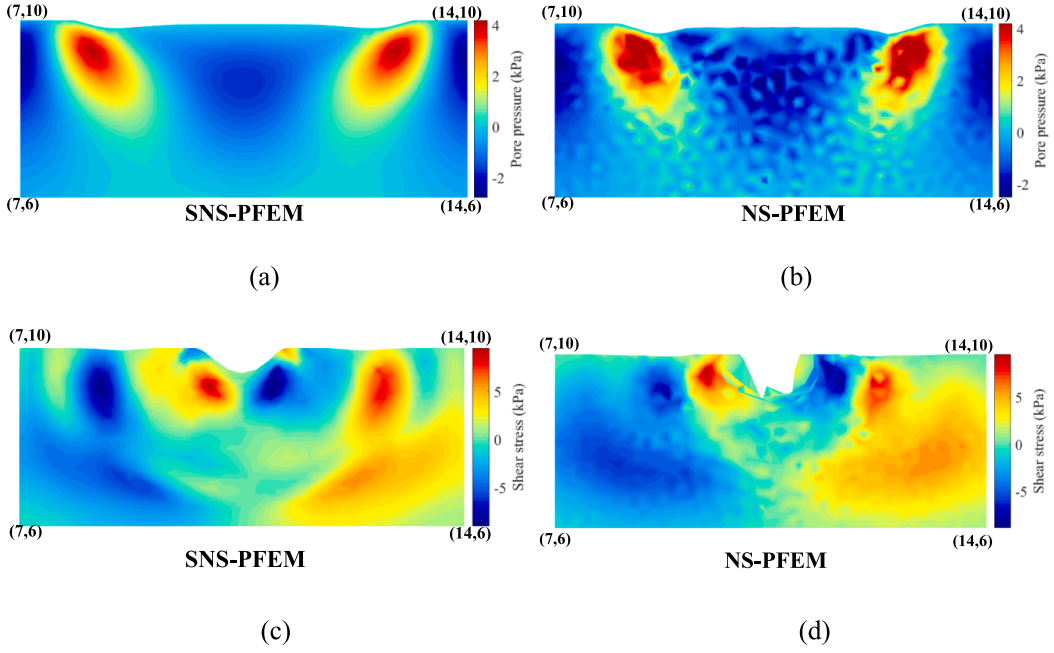

Fig. 16. Contour of pore pressure for the elastic case with (a) SNS-PFEM and (b) NS-PFEM; contours of shear stress for the elastoplastic case with (c) SNS-PFEM and (d) NS-PFEM.

$$P_{b,3} = \frac{\rho g H}{2\cosh(\lambda d)}\left[1 - \frac{\omega_2 \lambda^2 H^2}{2(U_0\lambda - \omega_0)}\right]\cos(\lambda x - \omega t) + \frac{3\pi\rho g H^2}{8L}\left[\frac{\omega_0(\omega_0 - U_0\lambda)}{2\sinh^4(\lambda d)} - \frac{g\lambda}{3\sinh(2\lambda d)}\right]\cos 2(\lambda x - \omega t) + \frac{3\rho\lambda H^3\omega_0(\omega_0 - U_0\lambda)}{512}\frac{9 - 4\sinh^2(\lambda d)}{\sinh^7(\lambda d)}\cos 3(\lambda x - \omega t) \tag{32}$$

$$\begin{cases} \omega = \omega_0 + (\lambda H)^2\omega_2 \\ \omega_0 = U_0\lambda + \sqrt{g\lambda \tanh \lambda d} \\ \omega_2 = \dfrac{(9 + 8\sinh^2(\lambda d) + 8\sinh^4(\lambda d))}{64\sinh^4(\lambda d)}(\omega_0 - U_0\lambda) \end{cases} \tag{33}$$

The first simulation is implemented on a 250 m wide and 200 m high region with the second-order stokes wave load. The geometry is discretized by 2997 nodes and 5792 elements. The related computational parameters are listed in the Table. 2, which takes the values from reference (Xu et al., 2017a). Along the vertical centre line, two monitoring points of depth 10 m (point A) and 100 m (point B) are set to record the evolution of vertical displacement and dynamic pore pressure. The results are exhibited in Fig. 21. Both the dynamic pore pressure and displacement oscillate at first due to the abruptly applied wave loading, and then become stable to a harmonic mode synchronously with the load. The dynamic responses decline with depth. Besides, the predictions of the SNS-PFEM and referenced FEM are in good consistency, although the latter uses a viscous-spring boundary. It verifies that a large geometry could decrease the influence of fixed boundaries.

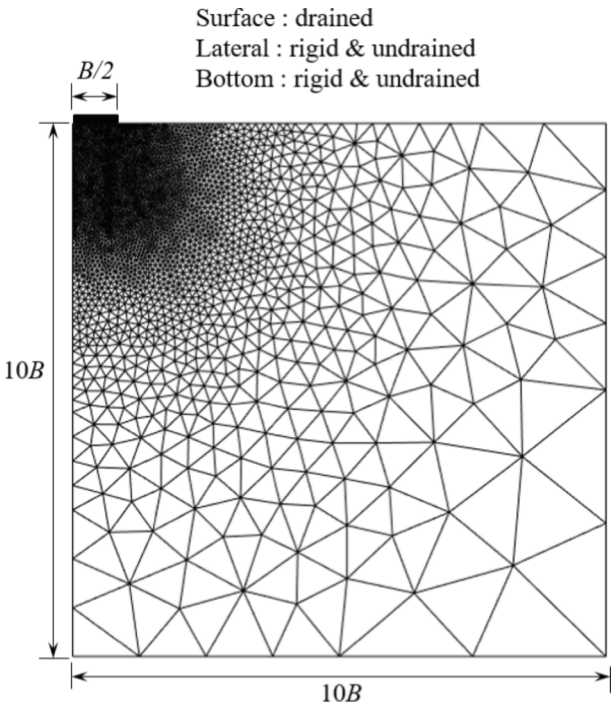

Fig. 17. Geometry and mesh of strip footing penetration on Mohr-Coulomb soil.

The second simulation is conducted using a 250 m wide and 30 m high region with the coupled third-order nonlinear wave and current pressure. A uniform mesh with 3559 nodes and 6888 elements is adopted. The related computational parameters are listed in the Table. 2, which takes the values from reference (Ye and Jeng, 2012). Fig. 22 presents the periodic distribution of the dynamic pore pressure and wave-induced vertical effective stress at $t = 20$ s, which agrees quite well with the referenced results (Ye and Jeng, 2012). Under the wave crest, the dynamic pore pressure is positive, and the dynamic vertical effective stress is compressive. It is just the opposite under the wave trough. According to the criterion in Eq. (34), the liquefication occurs at the position where the wave-induced vertical effective stress exceeds the original effective stress from the buoyant weight. Fig. 23 shows that with this criterion, the liquefication only happens at the top zone under the wave trough when the excess tensile tensile stress is large enough. The liquification zones move with the wave trough and would not stay somewhere permanently. This phenomenon is referred to as "transient liquefaction" in the poroelastic seabed, which has been identified in some model experiments (Chowdhury et al., 2006; Mory et al., 2007). The results validate that the proposed implicit SNS-PFEM is a reliable approach to simulate the dynamic problems of the seabed under wave and current loading.

$$\sigma'_{yd} \geqslant -(\gamma_s - \gamma_w)y \tag{34}$$

4.2. Simulation of the Selborne cutting slope

The Selborne experiment was implemented to provide a detailed record of the progressive failure of the slope of saturated high-plasticity clay (Cooper et al., 1998). As shown in Fig. 24, two layers of the weathered and unweathered Gault clays constitutes the 15 m high model, with the 9 m cutting made on the top weathered soil. The landslide is initiated by increasing the pore pressure on the boundary, which reduces the effective normal stress within the slope. The field was equipped with numerous of piezometers, extensometers and inclinometers to give precise surveying of the failure mechanism (Cooper et al., 1998). Such a problem may also be simulated with a quasi-static approach, while it is much better to include the dynamic effect to capture more realistic pre-rupture and post-failure phenomena with dynamic features (Soga et al., 2016). Because of the detailed benchmark field data, several large deformation numerical methods have modelled this experiment to validate their accuracy, such as the explicit MPM (Wang et al., 2021a, 2021b) and stabilized two-phase S-PFEM (Jin and Yin, 2022). The proposed SNS-PFEM uses the implicit generalized-α

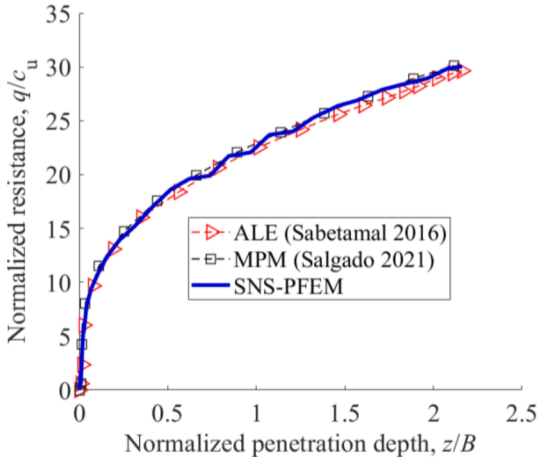

Fig. 19. Normalized soil resistance-penetration depth curve in the strip footing analysis.

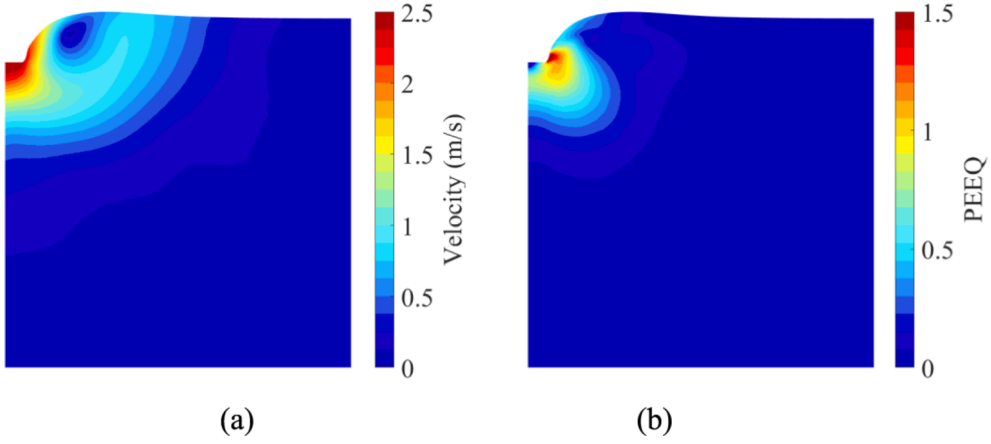

Fig. 18. Contour of (a) total velocity; (b) equivalent deviatoric plastic strain at the penetration depth of 2.5 m with SNS-PFEM.

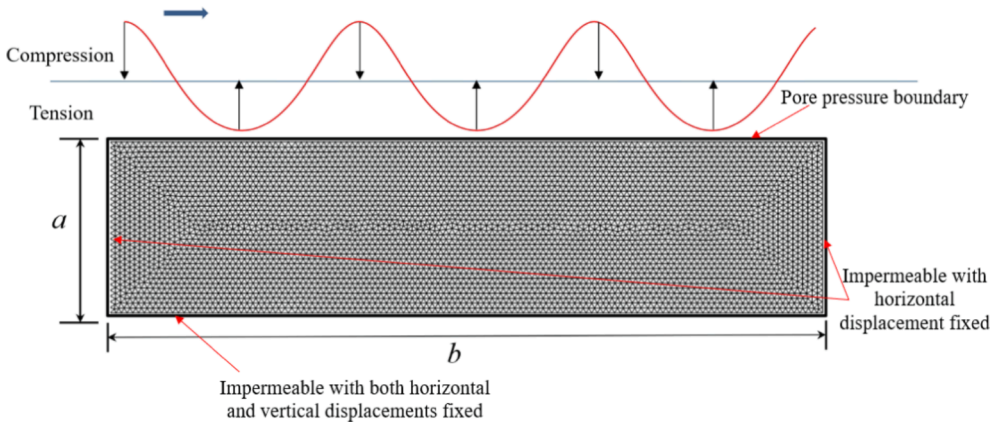

Fig. 20. Seabed under wave and current loading.

Table 2
Model parameters for the seabed under wave and current loading.

Parameter	Case 1 (Xu et al., 2017a)	Case 2 (Ye and Jeng, 2012)
Seabed height a (m)	200	30
Seabed width b (m)	250	250
Young's modulus E (MPa)	222.88	26.67
Poisson's ratio ν	0.4	0.33
Permeability (m/s)	1E−4	1E−4
Density of soil ρ(kg/m^3)	1800	1800
Density of water ρ_f(kg/m^3)	1000	1000
Wave number λ	0.0707	0.0739
Wave height H (m)	2	3
Wave depth d (m)	20	10
Wave length L (m)	88.88	85
Current velocity U_0 (m/s)	/	1
Time step Δt (s)	0.2	0.5

integration scheme with unconditional stability, which is superior to the explicit methods in the conditions of large time step and low permeability.

As shown in Fig. 24, a non-uniform mesh of 5252 nodes and 10,217 elements is used. The bottom boundary is undrained except the 24 m region for pore pressure loading. Both the weathered and unweathered Gault clay are simulated using the strain-softening Mohr-Coulomb (MC) model, where the friction angle ϕ and cohesion c are reduced with the accumulated equivalent plastic strain (PEEQ) as in Eqs. (35)–(37). Material properties are listed in the Table. 3, which are taken from references (Jin and Yin, 2022; Soga et al., 2016), except that the permeability is lowered to be more reasonable for the soft clay. The total computational period is set to $3 \times 10^5 s$ with the time step $\Delta t = 50$ s. The pore pressure 110 kPa is linearly applied in the first five time steps and then kept constant. The initial stress is generated by gravity loading with the soil density. It is well-known that the strain softening will increase the mesh dependency. This problem can be partly solved using some techniques, such as the smeared creak (Cervera and Chiumenti, 2006; Soga et al., 2016) or micropolar approaches (Deborst, 1993). In this study, the mesh size and softening parameters are directly taken from the references (Jin and Yin, 2022; Soga et al., 2016).

$$\phi = \psi = \phi_r + (\phi_p - \phi_r)e^{-\eta\varepsilon^p_{eq}} \tag{35}$$

$$c = c_r + (c_p - c_r)e^{-\eta\varepsilon^p_{eq}} \tag{36}$$

$$\varepsilon^p_{eq} = \sqrt{2(\boldsymbol{e}^p : \boldsymbol{e}^p)/3} \tag{37}$$

Fig. 25 presents the evolution of the contours of the horizontal displacement, equivalent deviatoric plastic strain and pore pressure together with the deformed geometry. The normalized time t^* is defined by the ratio of the real-time t and the critical failure time T: $t^* = t/T$. Due to the obvious difference in strengths of the weathered and unweathered soil, the failure mainly occurs in the top layer. With the boundary pore pressure reaching its peak value, the water starts to permeate and the pore pressure of the soil along the seepage path

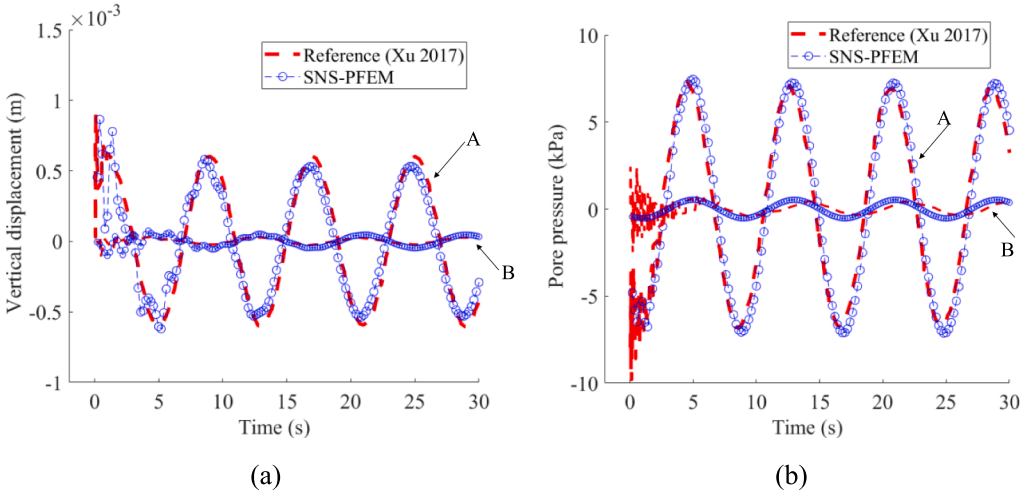

Fig. 21. Time histories of the (a) vertical displacement and (b) pore pressure at the monitoring points A and B under the second-order wave loading.

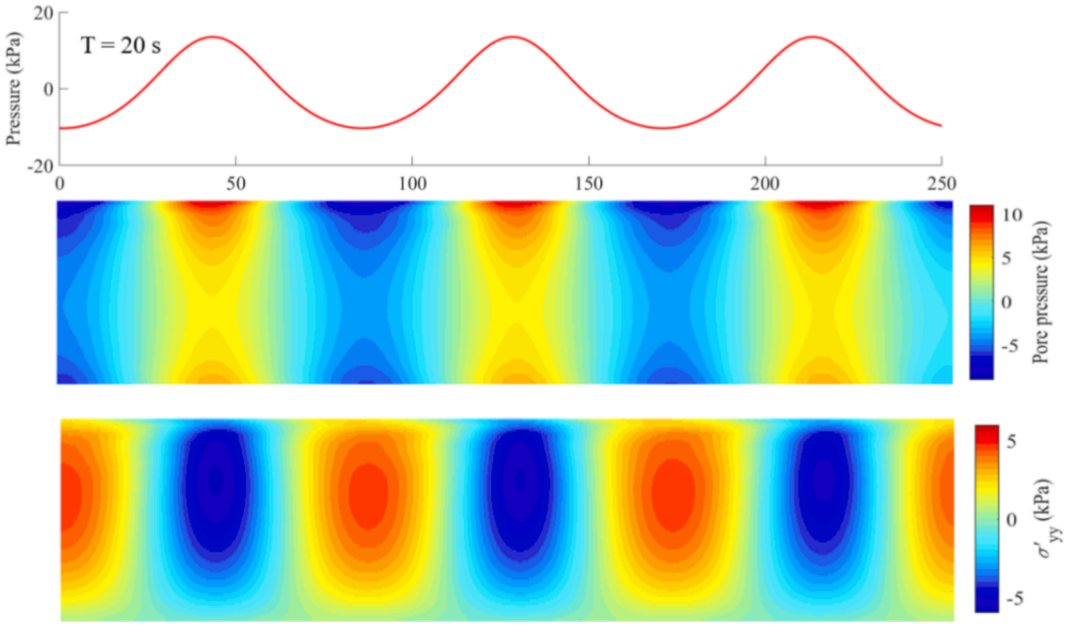

Fig. 22. Distribution of dynamic pore pressure and wave-induced vertical effective stress at time $t = 20$ s under the third-order wave loading.

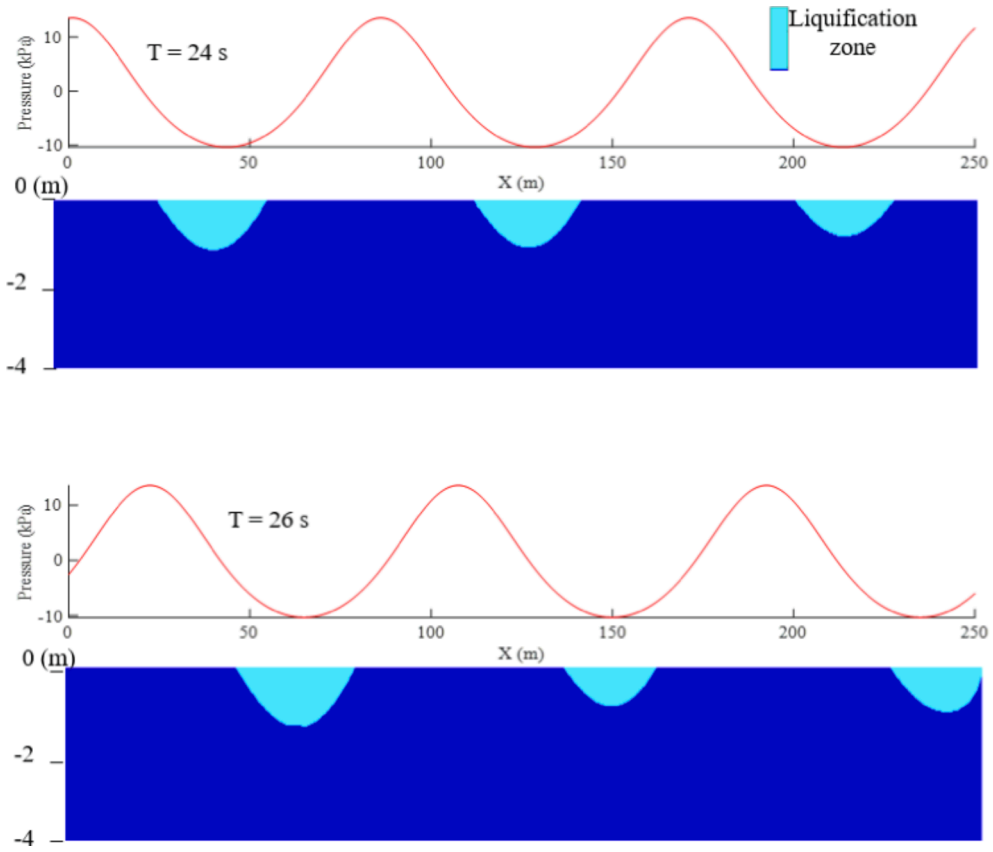

Fig. 23. Contours of liquefaction zones with the third-order wave loading at different scenarios $t = 24$ s and 26 s (the dimension of geometry is 250 m * 4 m).

increases. It can decrease the normal effective stress and leads to the initial yielding of some points near the slope top and toe. Then a clear sliding surface gets through rapidly. After that, the massive post-failure movement is triggered, and the sliding of the soil mass is accompanied by the expansion of the failure band, which shows the feature of a progressive failure mode. Fig. 26 (a) gives the comparison of the initial failure surface of the proposed dynamic SNS-PFEM with the referenced MPM and experimental results (Cooper et al., 1998; Jin and Yin, 2022; Soga et al., 2016). They are quite close to each other with some slight differences, which may come from the unavoidable distinction between the sophisticated real soil property and the simplified soil constitutive model.

Fig. 26 (b) exhibits the time history of the pore pressure at three monitoring points A, B and C, together with the results acquired by the

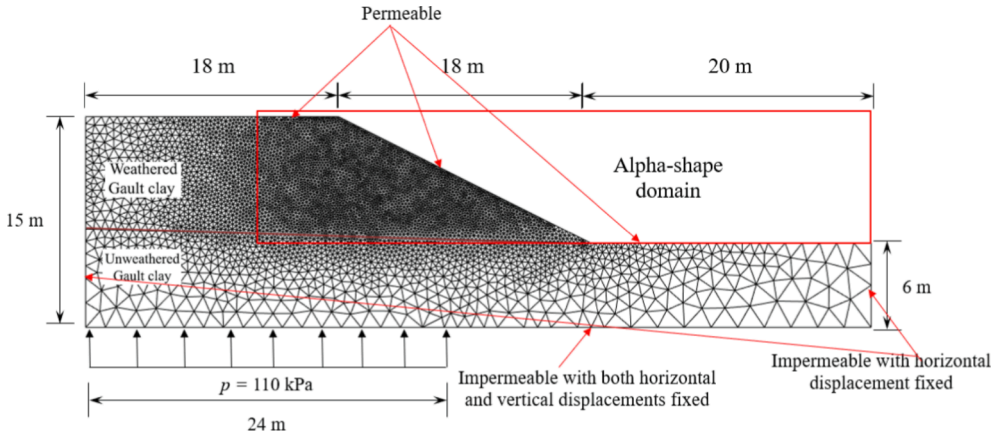

Fig. 24. Geometry and mesh of the Selborne cutting slope model.

Table 3
Properties of the soil constitutive model of the Selborne experiment.

Parameter	Weathered Gault clay	Unweathered Gault clay
Young's modulus E (MPa)	20	20
Poisson's ratio ν	0.33	0.33
Permeability (m/s)	1E−7	1E−7
Density of saturated soil ρ(kg/m^3)	1700	1700
Friction angle (peak/residual, °)	13/3.0	25/5.0
Cohesion c (peak/residual, kPa)	25/13.5	26/15
Shape factor of softening, η	400	400

referenced field experiment and MPM simulation. It shows that the results of SNS-PFEM are quite close to that of MPM, and also fall into reasonable agreement with the field data, especially at the piezometers A and B. The pore pressure of points A and B from both the numerical predictions and experimental results undergo a sudden drop when the failure occurs. This phenomenon contributed to the local volumetric extension state near the shear band (Soga et al., 2016).

Fig. 27 presents the evolution of the total displacements, velocities, and accelerations of three points D1, D2 and D3 at different heights. The movements of the three points are very slow during the first stage with the initial injection and seepage of water, which may correspond to elastic deformation, and then suddenly accelerate with the propagation of the failure zone. Point D3 near the slope toe reaches the static balance again soon after the global failure occurs, only experiencing a very small displacement. At the same time, point D1 near the top of the slope continues to run out at high speed and stops much later than point D3. All of the points undergo the stages of accelerating first and then decelerating, which depicts the whole process from the pre-failure to the post-failure. The asynchrony of the movements at different locations further validates the feature of progressive failure. The aforementioned results and comparisons demonstrate the accuracy of the proposed

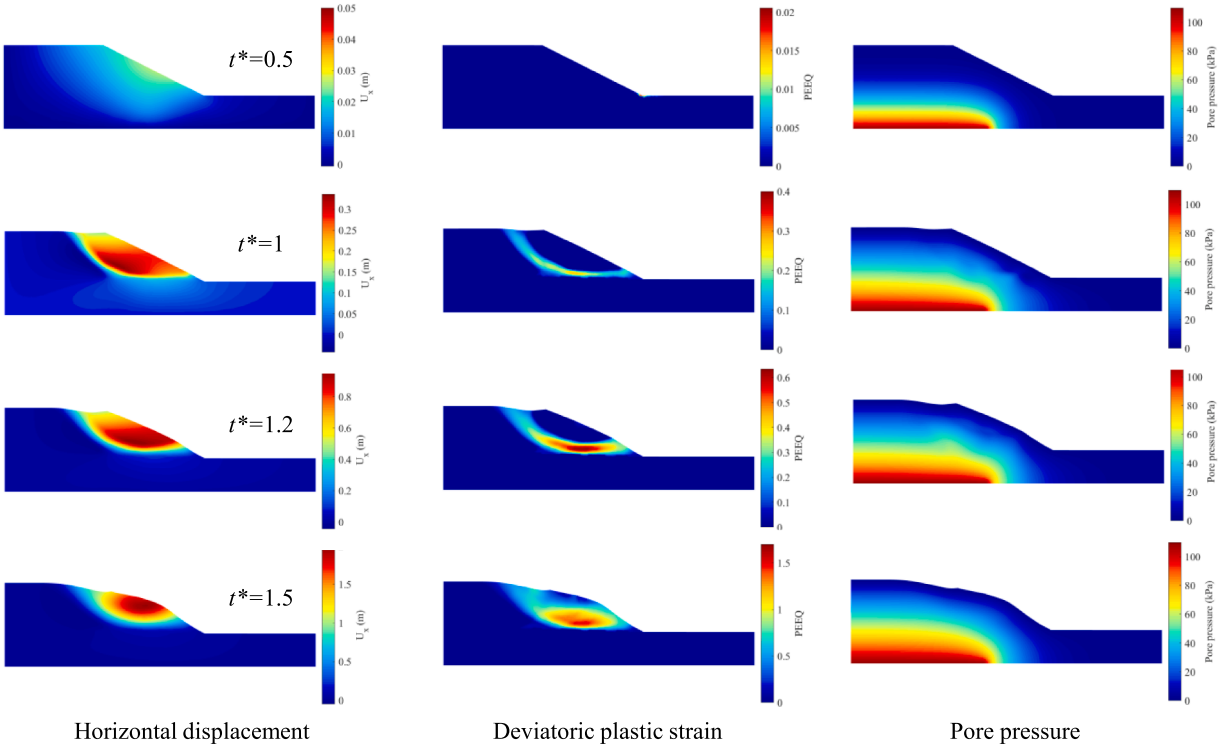

Fig. 25. Evolution of horizontal displacement, deviatoric plastic strain and pore pressure of the Selborne cutting slope with SNS-PFEM.

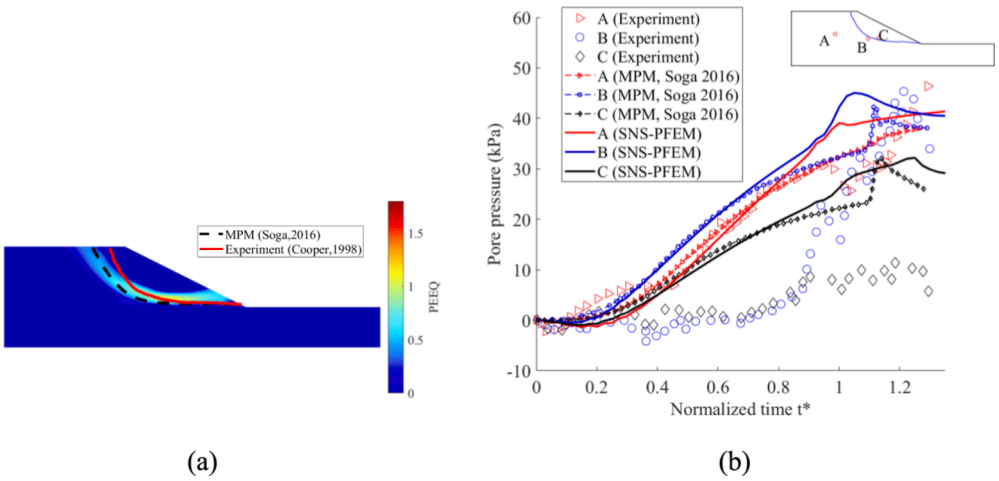

Fig. 26. (a) Comparison of the failure surfaces; (b) comparison of the evolution of pore pressure at the monitoring points A, B and C of SNS-PFEM with the experiment data and MPM simulation.

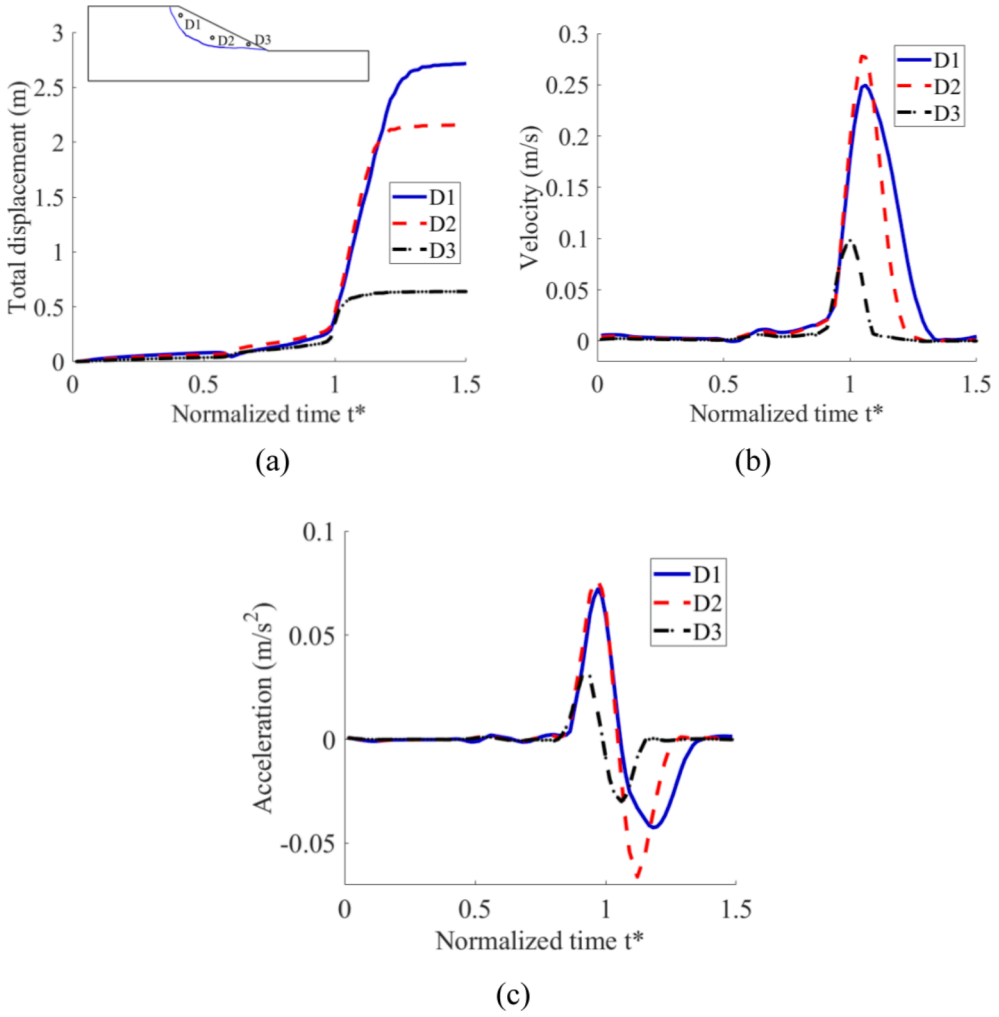

Fig. 27. Evolution of total displacement, velocity and acceleration at the monitoring points A, B and C of the Selborne cutting slope.

dynamic SNS-PFEM in simulating the realistic dynamic experiments of slope failure with large deformation.

4.3. Slope under seismic loading

The last example investigates the dynamic responses of a saturated slope under realistic seismic loading to illustrate the performance of the proposed SNS-PFEM in simulating the practical geotechnical hazards.

This kind of problem used to be explored by the total stress scheme with undrained assumptions. However, only with the hydro-mechanical coupled approach, some physical processes such as soil liquefaction and pore pressure evolution can be acquired. As shown in Fig. 28, the domain is discretised with a uniform mesh of 4094 nodes and 7837 elements. The soil is simulated with a strain-softening Tresca model as in Eqs. (35)–(37), where the parameters are set as in the Table. 4. The friction angle is set to 0 to simulate the pure cohesive clay. The seismic load is implemented by assigning the inertia force of earthquake acceleration to the slope, with the hyperbolic distribution of seismic coefficient as in Eq. (38), where a is the earthquake-induced acceleration, h is the height from the base and $D = 2H$ is the total height of the geometry. This coefficient is set to include the amplification effect from the ground basement to the surface (Wang et al., 2021a, 2021b). The EI Centro seismic acceleration in the north–south direction in Fig. 28 is treated as the input horizontal body force (Archuleta et al., 2006; Wang et al., 2021a, 2021b), which is magnified by a factor 1.3 to make the deformation more significant. The total computational period of 20 s with the time step $\Delta t = 0.02$ s is set. The step length takes the same value as the EI Centro seismic signal interval. The initial stress is generated by gravity loading with the soil density.

$$a_h = a\left(1 + 2(h/D)^2\right) \tag{38}$$

The failure mode of the saturated slope subjected to seismic loading is presented in Fig. 29 (a). Firstly, a main plastic zone is formed at the bottom under the slope toe, with several small failure bands appearing behind it. All the failure bands start from the bottom and propagate towards the ground. Then, two intersecting straight faults and one single curved failure band get through the ground surface, forming an active wedge block behind the curved failure band. Finally, a clear quasi-circular slip surface gets through. The sliding body forms and suffers a large movement, presenting a typical deep failure mode of the cohesive soil slope. The earthquake-induced pore pressure experiences an obvious redistribution caused by the failure bands, as shown in Fig. 29 (b). The velocity and acceleration at $t = 20$ s before and after applying the α-shape method are plotted in Fig. 30. For the sliding body, the maximum velocity appears along the quasi-circular slip surface and decreases towards the ground surface, presenting a rotation pattern. For the active wedge block, however, the maximum velocity occurs on the ground surface and decreases towards the bottom. As shown in Fig. 30, the soils on the top and along the failure bands have greater acceleration. This distribution may be caused by the fixed bottom and hyperbolic seismic coefficient in Eq. (38). The earthquake-induced multiple shear bands can also be observed in the previous study for the slope in sensitive clay (Wang et al., 2021a, 2021b). The variable redistribution before and after the remeshing process is not significant, except in some boundary regions where the unreasonable elements are deleted. In the SNS-PFEM, the variables are directly carried by the nodes (particles), thus variable mapping will not be used. This feature benefits in reducing the accuracy loss in the remeshing process. All the results indicate that the proposed dynamic coupled SNS-PFEM can effectively simulate the whole process of the earthquake-induced slope failure with large deformation.

Table 4
Properties of the soil constitutive model of slope under seismic loading.

Parameters	Clay
Young's modulus E (MPa)	20
Poisson's ratio ν	0.3
Permeability (m/s)	1E−7
Density of saturated soil ρ(kg/m^3)	1700
Cohesion c (peak/residual, kPa)	60/12
Shape factor of softening, η	100

5. Conclusions

This study proposed a dynamic hydro-mechanical coupled SNS-PFEM for analysing saturated porous medium with the u-p format. The subdomain-based stress point stabilization was adopted to circumvent the spurious non-zero energy mode of direct nodal integration in the dynamic Galerkin weak forms. The polynomial pressure projection (PPP) technique was implemented to accommodate the dynamic hydro-mechanical coupled formulations, aiming to overcome the unphysical pore pressure oscillation in the low-permeability limit. The step-by-step time integration algorithm based on the CH generalized-α method was derived, leading to an unconditionally stable implicit solution scheme.

Five benchmark examples were simulated to validate the accuracy and efficiency of the proposed method, namely the free vibration of a shear wall, the elastoplastic beam under a sudden load, the 1D dynamic consolidation, the 2D wave propagation and the strip footing penetration. The required dynamic responses are in good consistency with the reference solutions in both elastic and elastoplastic, uncoupled and coupled conditions. The polynomial pressure projection was proved to be effective in stabilizing the undrained pore pressure oscillation. The nodal integration stabilization can help correct the overly soft defect in

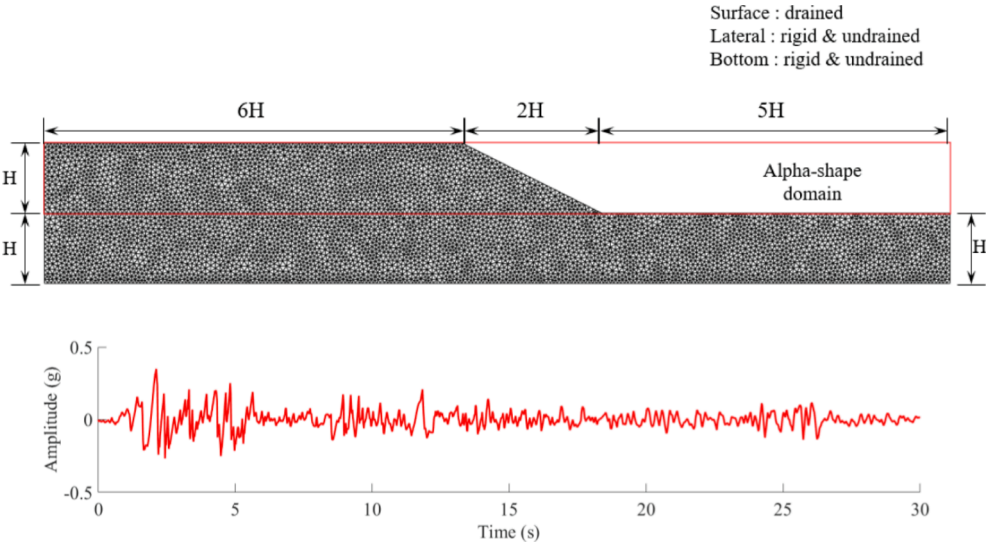

Fig. 28. Geometry and mesh of the slope with the seismic signal of 1940 EI Centro earthquake.

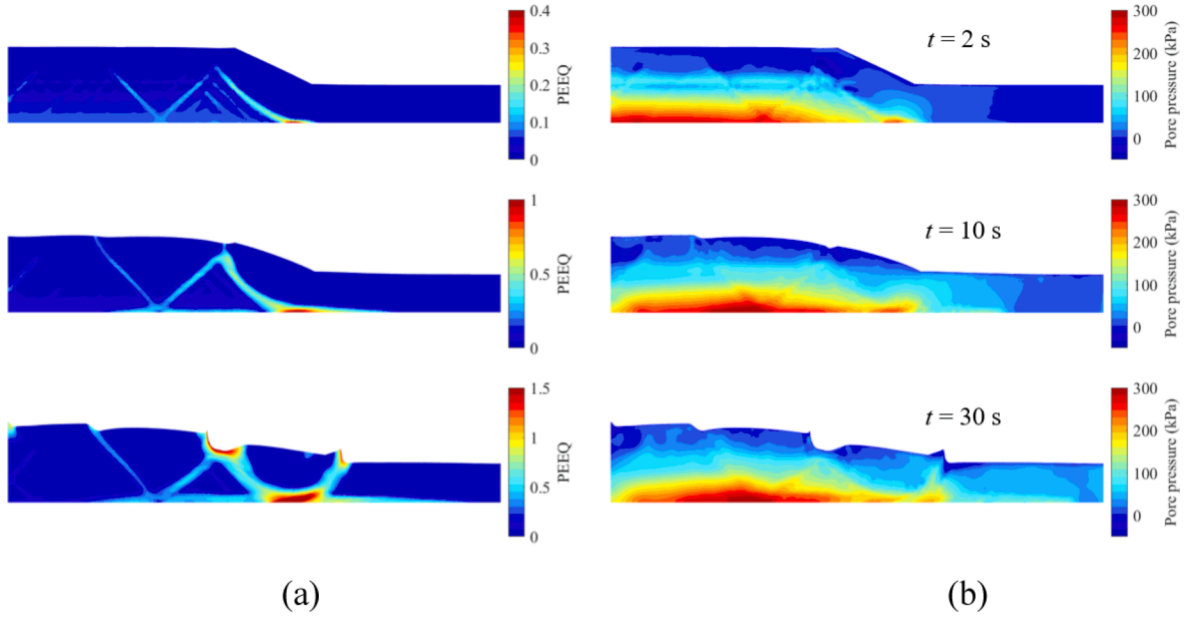

Fig. 29. (a) Contour of deviatoric plastic strain; (b) contour of pore pressure of the slope under seismic loading at different time.

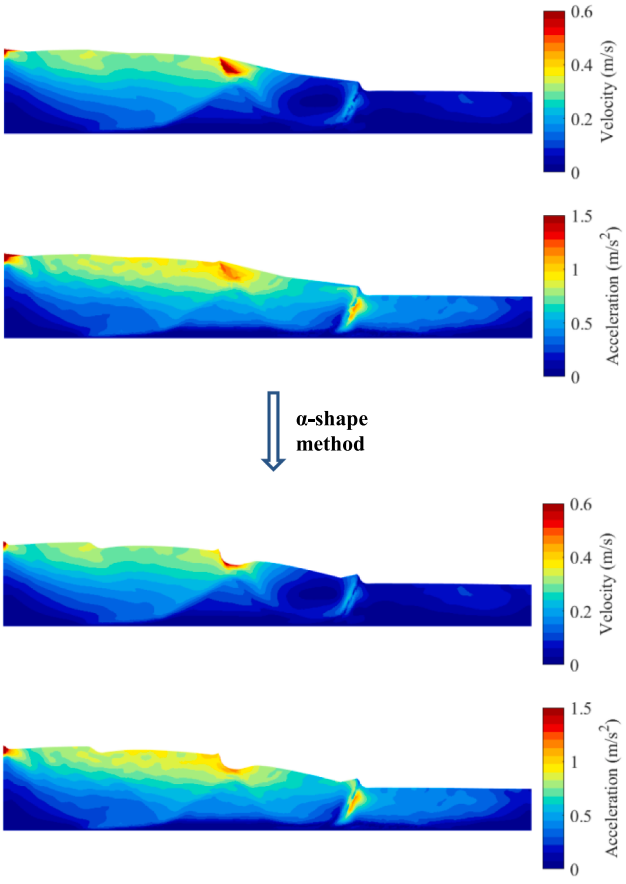

Fig. 30. Contour of total velocity and acceleration at $t = 20$ s (before and after applying the α-shape method).

vibration mode and eigenvalue analysis, and also cure the temporal instability in calculating dynamic responses with time integration scheme.

The proposed method was further applied to simulate some more sophisticated geotechnical dynamic problems, i.e., the elastic seabed under wave and current, the Selborne slope failure experiment, and the slope under real seismic loading. The results are reasonable and in good accordance with the experimental data and reference solutions. Some dynamic features, such as the transient liquefaction of the seabed and the progressive failure of a saturated slope, can be correctly depicted, which indicates that the proposed SNS-PFEM is reliable in modelling the hydro-mechanical coupled problems with realistic dynamic loading and large deformation.

Several limitations still exist in the current coupled dynamic SNS-PFEM, which could lead to some future work. First, the *u-p* format neglects the relative acceleration of fluid to the solid skeleton. This assumption only holds in the low-frequency conditions. It seems worthwhile to develop the *u-U* or *u-w-p* formats in SNS-PFEM to obtain more realistic dynamic responses in high-frequency conditions. Second, some dynamic constitutive models of soils such as PDMY can be implemented in this code (Iwan, 1967), to simulate the displacement accumulation or liquefaction under cyclic loading. Moreover, the current SNS-PFEM is two-dimensional, which can be further extended to a three-dimensional version in a simple manner.

CRediT authorship contribution statement

Ze-Yu Wang: Methodology, Software, Validation, Formal analysis, Investigation, Data curation, Writing – original draft. **Yin-Fu Jin:** Conceptualization, Methodology, Software, Supervision, Investigation, Data curation, Writing – review & editing. **Zhen-Yu Yin:** Resources, Conceptualization, Methodology, Writing – review & editing, Supervision, Project administration, Funding acquisition. **Yu-Ze Wang:** Conceptualization, Supervision, Resources, Methodology, Writing – review & editing.

Declaration of Competing Interest

The authors declare that they have no known competing financial interests or personal relationships that could have appeared to influence the work reported in this paper.

Data availability

Data will be made available on request.

Acknowledgements

This research is financially supported by the National Natural Science Foundation of China (Grant No. 52278363), the Hong Kong Polytechnic University Strategic Importance Fund (ZE2T) and Project of Research Institute of Land and Space (CD78) and the Research Grants Council (RGC) of Hong Kong Special Administrative Region Government (HKSARG) of China (Grant No.: R5037-18F).

Appendix A

A.1. Formulations of dynamic finite element equations

The consistent mass matrix $\mathbf{M}$ is defined in Eq. (39), where ρ is the density of mixture used in Eq. (1), and $\boldsymbol{N}_u$ is the displacement interpolation matrix. The mass matrix of linear triangular element can also be lumped to a diagonalized form to save computational cost, which has been widely adopted in FEM practice.

$$\boldsymbol{M} = \int_{\Omega} \rho \boldsymbol{N}_u^T \boldsymbol{N}_u d\Omega \tag{39}$$

$$\boldsymbol{N}_u = [\boldsymbol{N}_{u,1} \quad \boldsymbol{N}_{u,2} \quad \dots \quad \boldsymbol{N}_{u,n}] = \begin{bmatrix} N_1 & 0 & N_2 & 0 & \dots & N_n & 0 \\ 0 & N_1 & 0 & N_2 & \dots & 0 & N_n \end{bmatrix} \tag{40}$$

The internal force $\boldsymbol{F}^{ints}$ from the effective stress is presented in Eq. (41), where the gradient $\boldsymbol{B}_u$ is defined in Eq. (43). The stiffness matrix $\boldsymbol{K}_{uu}$ in Eq. (42) is calculated by taking the derivative of internal force to the displacement.

$$\boldsymbol{F}^{ints}(\boldsymbol{U}) = \int_{\Omega} \boldsymbol{B}_u^T \boldsymbol{\sigma}' d\Omega \tag{41}$$

$$\boldsymbol{K}_{uu} = \frac{\partial \boldsymbol{F}^{ints}(\boldsymbol{U})}{\partial \boldsymbol{U}} = \int_{\Omega} \boldsymbol{B}_u^T \boldsymbol{D} \boldsymbol{B}_u d\Omega \tag{42}$$

$$\boldsymbol{B}_u = \boldsymbol{L}_d \boldsymbol{N}_u = [\boldsymbol{B}_{u,1} \quad \boldsymbol{B}_{u,2} \quad \dots \quad \boldsymbol{B}_{u,n}], \ \boldsymbol{L}_d = \begin{bmatrix} \frac{\partial}{\partial x} & 0 & \frac{\partial}{\partial y} \\ 0 & \frac{\partial}{\partial y} & \frac{\partial}{\partial x} \end{bmatrix}^T \tag{43}$$

The permeability matrix $\boldsymbol{K}_{pp}$ and coupling matrix $\boldsymbol{K}_{up}$ are defined in Eqs. (44)–(49).

$$\boldsymbol{K}_{pp} = \int_{\Omega} \boldsymbol{B}_p^T \boldsymbol{k}_f \boldsymbol{B}_p d\Omega \tag{44}$$

$$\boldsymbol{K}_{up} = \int_{\Omega} \boldsymbol{B}_u^T \boldsymbol{m} \boldsymbol{N}_p d\Omega \tag{45}$$

$$\boldsymbol{k}_f = \frac{1}{\gamma_f} \begin{bmatrix} k_x & 0 \\ 0 & k_y \end{bmatrix} \tag{46}$$

$$\boldsymbol{m} = [1 \quad 1 \quad 0]^T \tag{47}$$

$$\boldsymbol{N}_p = [\boldsymbol{N}_{p,1} \quad \boldsymbol{N}_{p,2} \quad \dots \quad \boldsymbol{N}_{p,n}] = [N_1 \quad N_2 \quad \dots \quad N_n] \tag{48}$$

$$\boldsymbol{B}_p = \boldsymbol{L}_f \boldsymbol{N}_p = [\boldsymbol{B}_{p,1} \quad \boldsymbol{B}_{p,2} \quad \dots \quad \boldsymbol{B}_{p,n}], \ \boldsymbol{L}_f = \begin{bmatrix} \frac{\partial}{\partial x} & \frac{\partial}{\partial y} \end{bmatrix}^T \tag{49}$$

The external load vector $\boldsymbol{F}^{ext}$ and flow flux term $\boldsymbol{Q}^{ext}$ are defined in Eqs. (50)–(51).

$$\boldsymbol{F}^{ext} = \int_{\Gamma_t} \boldsymbol{N}_u^T \bar{\boldsymbol{t}} d\Gamma + \int_{\Omega} \boldsymbol{N}_u^T \boldsymbol{f} d\Omega \tag{50}$$

$$\boldsymbol{Q}^{ext} = \int_{\Gamma_q} \boldsymbol{N}_p^T \bar{q} d\Gamma \tag{51}$$

For simplicity, the Rayleigh damping is used in this numerical framework, where the damping matrix $\boldsymbol{C}$ is the linear combination of the stiffness matrix $\boldsymbol{K}_{uu}$ and mass matrix $\boldsymbol{M}$ with the Rayleigh damping coefficients a_1 and a_2.

$$\boldsymbol{C} = a_1 \boldsymbol{M} + a_2 \boldsymbol{K}_{uu} \tag{52}$$

A.2. Derivation of hydro-mechanical coupled CH generalized-α method with PPP

The following variants of Newmark-β method are presented in Eqs. (53)–(55). In Eq. (54), the velocity and acceleration at t_{n+1} are expressed as the function of displacement at t_{n+1} and other known variables at t_n. In Eq. (55), the incremental velocity and acceleration are expressed as the function of the incremental displacement and other known variables at t_n.

$$\begin{cases} \boldsymbol{U}_{t_{n+1}} = \left(\boldsymbol{U}_{t_n} + \dot{\boldsymbol{U}}_{t_n}\Delta t + (\frac{1}{2}-\beta)\ddot{\boldsymbol{U}}_{t_n}\Delta t^2\right) + \beta\ddot{\boldsymbol{U}}_{t_{n+1}}\Delta t^2 = \boldsymbol{A}_{t_n} + \beta\ddot{\boldsymbol{U}}_{t_{n+1}}\Delta t^2 \\ \dot{\boldsymbol{U}}_{t_{n+1}} = \left(\dot{\boldsymbol{U}}_{t_n} + (1-\gamma)\ddot{\boldsymbol{U}}_{t_n}\Delta t\right) + \gamma\ddot{\boldsymbol{U}}_{t_{n+1}}\Delta t = \boldsymbol{B}_{t_n} + \gamma\ddot{\boldsymbol{U}}_{t_{n+1}}\Delta t \end{cases} \tag{53}$$

$$\begin{cases} \ddot{\boldsymbol{U}}_{t_{n+1}} = \dfrac{1}{\beta\Delta t^2}(\boldsymbol{U}_{t_{n+1}} - \boldsymbol{A}_{t_n}) \\ \dot{\boldsymbol{U}}_{t_{n+1}} = \boldsymbol{B}_{t_n} + \dfrac{\gamma}{\beta\Delta t}(\boldsymbol{U}_{t_{n+1}} - \boldsymbol{A}_{t_n}) \end{cases} \tag{54}$$

$$\begin{cases} \ddot{\boldsymbol{U}}_{t_{n+1}} - \ddot{\boldsymbol{U}}_{t_n} = \dfrac{1}{\beta\Delta t^2}(\boldsymbol{U}_{t_{n+1}} - \boldsymbol{U}_{t_n}) - \dfrac{1}{\beta\Delta t}\dot{\boldsymbol{U}}_{t_n} - \dfrac{1}{2\beta}\ddot{\boldsymbol{U}}_{t_n} \\ \dot{\boldsymbol{U}}_{t_{n+1}} - \dot{\boldsymbol{U}}_{t_n} = \ddot{\boldsymbol{U}}_{t_n}\Delta t + \gamma\Delta t(\ddot{\boldsymbol{U}}_{t_{n+1}} - \ddot{\boldsymbol{U}}_{t_n}) = \dfrac{\gamma}{\beta\Delta t}(\boldsymbol{U}_{t_{n+1}} - \boldsymbol{U}_{t_n}) - \dfrac{\gamma}{\beta}\dot{\boldsymbol{U}}_{t_n} - \left(\dfrac{\gamma}{2\beta} - 1\right)\ddot{\boldsymbol{U}}_{t_n} \end{cases} \tag{55}$$

The Eq. (56) is acquired by substituting the Eqs. (53)–(55) into the equilibrium Eq. (26). Noticing that the effective internal force is integrated at $t_{n+1-\alpha_f}$ and the effective stress needs to be updated at t_{n+1}, the constitutive model should be integrated twice at each Newton-Raphson iteration. The Eq. (57) is further converted to the Eq. (58) by eliminating all the first and second-order derivatives at t_{n+1}, so as to arrive at the standard FEM equations with nodal variable increments.

$$\begin{aligned} &\boldsymbol{M}\ddot{\boldsymbol{U}}_{t_{n+1-\alpha_m}} + \overline{\boldsymbol{C}}\dot{\boldsymbol{U}}_{t_{n+1-\alpha_f}} + \overline{\boldsymbol{F}}^{ints}\left(\boldsymbol{U}_{t_n} + (1-\alpha_f)(\boldsymbol{U}_{t_{n+1}} - \boldsymbol{U}_{t_n})\right) \\ &\quad - \overline{\boldsymbol{F}}^{ints}(\boldsymbol{U}_{t_n}) - \overline{\boldsymbol{K}}_{up}\boldsymbol{P}_{t_{n+1-\alpha_f}} = \boldsymbol{F}^{ext}_{t_{n+1-\alpha_f}} - \overline{\boldsymbol{F}}^{ints}(\boldsymbol{U}_{t_n}) \end{aligned} \tag{56}$$

$$\begin{aligned} &(1-\alpha_m)\boldsymbol{M}(\ddot{\boldsymbol{U}}_{t_{n+1}} - \ddot{\boldsymbol{U}}_{t_n}) + (1-\alpha_f)\overline{\boldsymbol{C}}(\dot{\boldsymbol{U}}_{t_{n+1}} - \dot{\boldsymbol{U}}_{t_n}) \\ &+\left(\overline{\boldsymbol{F}}^{ints}\left(\boldsymbol{U}_{t_n} + (1-\alpha_f)(\boldsymbol{U}_{t_{n+1}} - \boldsymbol{U}_{t_n})\right) - \overline{\boldsymbol{F}}^{ints}(\boldsymbol{U}_{t_n})\right) - (1-\alpha_f)\overline{\boldsymbol{K}}_{up}(\boldsymbol{P}_{t_{n+1}} - \boldsymbol{P}_{t_n}) \\ &= \alpha_f\boldsymbol{F}^{ext}_{t_n} + (1-\alpha_f)\boldsymbol{F}^{ext}_{t_{n+1}} - \boldsymbol{M}\ddot{\boldsymbol{U}}_{t_n} - \overline{\boldsymbol{C}}\dot{\boldsymbol{U}}_{t_n} - \overline{\boldsymbol{F}}^{ints}(\boldsymbol{U}_{t_n}) + \overline{\boldsymbol{K}}_{up}\boldsymbol{P}_{t_n} \\ &= (1-\alpha_f)\left(\boldsymbol{F}^{ext}_{t_{n+1}} - \boldsymbol{F}^{ext}_{t_n}\right) \end{aligned} \tag{57}$$

$$\begin{aligned} &\left(\frac{1-\alpha_m}{\beta\Delta t^2}\boldsymbol{M} + \frac{(1-\alpha_f)\gamma}{\beta\Delta t}\overline{\boldsymbol{C}}\right)(\boldsymbol{U}_{t_{n+1}} - \boldsymbol{U}_{t_n}) + \left(\overline{\boldsymbol{F}}^{ints}\left(\boldsymbol{U}_{t_n} + (1-\alpha_f)(\boldsymbol{U}_{t_{n+1}} - \boldsymbol{U}_{t_n})\right) - \overline{\boldsymbol{F}}^{ints}(\boldsymbol{U}_{t_n})\right) \\ &-(1-\alpha_f)\overline{\boldsymbol{K}}_{up}(\boldsymbol{P}_{t_{n+1}} - \boldsymbol{P}_{t_n}) = (1-\alpha_f)\left(\boldsymbol{F}^{ext}_{t_{n+1}} - \boldsymbol{F}^{ext}_{t_n}\right) + (1-\alpha_m)\boldsymbol{M}\left(\frac{1}{\beta\Delta t}\dot{\boldsymbol{U}}_{t_n} + \frac{1}{2\beta}\ddot{\boldsymbol{U}}_{t_n}\right) \\ &\quad +(1-\alpha_f)\overline{\boldsymbol{C}}\left(\frac{\gamma}{\beta}\dot{\boldsymbol{U}}_{t_n} + \left(\frac{\gamma}{2\beta} - 1\right)\ddot{\boldsymbol{U}}_{t_n}\Delta t\right) \end{aligned} \tag{58}$$

The Eq. (59) is acquired by substituting the Eqs. (24) into the mass conservation Eq. (26) and then converting it into the incremental format.

$$\begin{aligned} &\overline{\boldsymbol{K}}^T_{up}(\boldsymbol{U}_{t_{n+1}} - \boldsymbol{U}_{t_n}) + \left(\theta\Delta t\overline{\boldsymbol{K}}_{pp} + \boldsymbol{S}\right)(\boldsymbol{P}_{t_{n+1}} - \boldsymbol{P}_{t_n}) \\ &= (\alpha_f\boldsymbol{Q}^{ext}_{t_n} + (1-\alpha_f)\boldsymbol{Q}^{ext}_{t_{n+1}})\Delta t - \overline{\boldsymbol{K}}_{pp}\boldsymbol{P}_{t_n}\Delta t \end{aligned} \tag{59}$$

Finally, the nonlinear Eq. (26) is solved by the standard Newton-Raphson procedure. The linearized equations, the variable updating rules and the residual formulations at the ith iteration from t_n to t_{n+1} are exhibited in Eqs. (60)–(66). The iteration will automatically stop when the pre-set convergence criterion is satisfied.

$$\begin{bmatrix} \widehat{\boldsymbol{K}}_{uu} & -(1-\alpha_f)\overline{\boldsymbol{K}}_{up} \\ -(1-\alpha_f)\overline{\boldsymbol{K}}^T_{up} & -(1-\alpha_f)\left(\theta\Delta t\overline{\boldsymbol{K}}_{pp} + \boldsymbol{S}\right) \end{bmatrix}_{t_{n+1}} \begin{bmatrix} \delta\boldsymbol{U} \\ \delta\boldsymbol{P} \end{bmatrix}^{(i)}_{t_{n+1}} = \begin{bmatrix} \Delta\boldsymbol{R}_u \\ \Delta\boldsymbol{R}_p \end{bmatrix}^{(i)}_{t_{n+1}} \tag{60}$$

$$\widehat{\boldsymbol{K}}_{uu} = \frac{1-\alpha_m}{\beta\Delta t^2}\boldsymbol{M} + \frac{(1-\alpha_f)\gamma}{\beta\Delta t}\overline{\boldsymbol{C}} + (1-\alpha_f)\overline{\boldsymbol{K}}_{uu} \tag{61}$$

$$\begin{bmatrix} \Delta\boldsymbol{U} \\ \Delta\boldsymbol{P} \end{bmatrix}^{(i)}_{t_{n+1}} = \begin{bmatrix} \Delta\boldsymbol{U} \\ \Delta\boldsymbol{P} \end{bmatrix}^{(i-1)}_{t_{n+1}} + \begin{bmatrix} \delta\boldsymbol{U} \\ \delta\boldsymbol{P} \end{bmatrix}^{(i)}_{t_{n+1}} \tag{62}$$

$$\begin{bmatrix} \Delta\boldsymbol{U} \\ \Delta\boldsymbol{P} \end{bmatrix}^{(0)}_{t_{n+1}} = \begin{bmatrix} 0 \\ 0 \end{bmatrix} \tag{63}$$

$$\begin{bmatrix} \boldsymbol{U} \\ \boldsymbol{P} \end{bmatrix}_{t_{n+1}} = \begin{bmatrix} \boldsymbol{U} \\ \boldsymbol{P} \end{bmatrix}_{t_n} + \begin{bmatrix} \Delta\boldsymbol{U} \\ \Delta\boldsymbol{P} \end{bmatrix}_{t_{n+1}} \tag{64}$$

$$
\begin{aligned}
&(\Delta \boldsymbol{R}_u)_{t_{n+1}}^{(i)} = (1-\alpha_f)\left(\boldsymbol{F}_{t_{n+1}}^{ext} - \boldsymbol{F}_{t_n}^{ext}\right) + (1-\alpha_m)\boldsymbol{M}\left(\frac{1}{\beta\Delta t}\dot{\boldsymbol{U}}_{t_n} + \frac{1}{2\beta}\ddot{\boldsymbol{U}}_{t_n}\right) \\
&+(1-\alpha_f)\overline{\boldsymbol{C}}\left(\frac{\gamma}{\beta}\dot{\boldsymbol{U}}_{t_n} + \left(\frac{\gamma}{2\beta}-1\right)\ddot{\boldsymbol{U}}_{t_n}\Delta t\right) - \left(\frac{1-\alpha_m}{\beta\Delta t^2}\boldsymbol{M} + \frac{(1-\alpha_f)\gamma}{\beta\Delta t}\boldsymbol{C}\right)\left(\boldsymbol{U}_{t_{n+1}}^{(i-1)} - \boldsymbol{U}_{t_n}\right) \\
&-\left(\overline{\boldsymbol{F}}^{ints}\left(\boldsymbol{U}_{t_n} + (1-\alpha_f)(\boldsymbol{U}_{t_{n+1}}^{(i-1)} - \boldsymbol{U}_{t_n})\right) - \overline{\boldsymbol{F}}^{ints}(\boldsymbol{U}_{t_n})\right) + (1-\alpha_f)\overline{\boldsymbol{K}}_{up}(\boldsymbol{P}_{t_{n+1}}^{(i-1)} - \boldsymbol{P}_{t_n})
\end{aligned} \tag{65}
$$

$$
\begin{aligned}
\left(\Delta \boldsymbol{R}_p\right)_{t_{n+1}}^{(i)} &= (1-\alpha_f)\left(\overline{\boldsymbol{K}}_{pp}\boldsymbol{P}_{t_n}\Delta t - (\alpha_f\boldsymbol{Q}_{t_n}^{ext} + (1-\alpha_f)\boldsymbol{Q}_{t_{n+1}}^{ext})\Delta t\right) \\
&+\overline{\boldsymbol{K}}_{up}^{T}(\boldsymbol{U}_{t_{n+1}}^{(i-1)} - \boldsymbol{U}_{t_n}) + \left(\theta\Delta t\overline{\boldsymbol{K}}_{pp} + \boldsymbol{S}\right)\left(\boldsymbol{P}_{t_{n+1}}^{(i-1)} - \boldsymbol{P}_{t_n}\right)
\end{aligned} \tag{66}
$$

References

Andersen, S., Andersen, L., 2010. Modelling of landslides with the material-point method. Comput. Geosci. 14 (1), 137–147.

Archuleta, R.J., Steidl, J., Squibb, M., 2006. The COSMOS Virtual Data Center: a web portal for strong motion data dissemination. Seismol. Res. Lett. 77 (6), 651–658.

Belytschko, T., Lu, Y.Y., Gu, L., 1994. Element-free Galerkin methods. Int. J. Numer. Meth. Eng. 37 (2), 229–256.

Belytschko, T., Krongauz, Y., Organ, D., et al., 1996. Meshless methods: an overview and recent developments. Comput. Meth. Appl. Mech. Eng. 139 (1–4), 3–47.

Biot, M.A., 1956a. Theory of propagation of elastic waves in a fluid-saturated porous solid. 1. Low-frequency range. J. Acoust. Soc. Am. 28 (2), 168–178.

Biot, M.A., 1956b. Theory of propagation of elastic waves in a fluid-saturated porous solid. 2. Higher frequency range. J. Acoust. Soc. Am. 28 (2), 179–191.

Biot, M.A., 1962. Mechanics of deformation and acoustic propagation in porous media. J. Appl. Phys. 33 (4), 1482–1490.

Brebbia, C.A., 1984. Boundary Element Techniques. Springer Verlag, Berlin.

Brezzi, F., Bathe, K.J., 1990. A discourse on the stability conditions for mixed finite-element formulations. Comput. Meth. Appl. Mech. Eng. 82 (1–3), 27–57.

Bui, H.H., Fukagawa, R., 2013. An improved SPH method for saturated soils and its application to investigate the mechanisms of embankment failure: case of hydrostatic pore-water pressure. Int. J. Numer. Anal. Meth. Geomech. 37 (1), 31–50.

Bui, H.H., Nguyen, G.D., 2017. A coupled fluid-solid SPH approach to modelling flow through deformable porous media. Int. J. Solids Struct. 125, 244–264.

Carbonell, J.M., Monforte, L., Ciantia, M.O., et al., 2022. Geotechnical particle finite element method for modeling of soil-structure interaction under large deformation conditions. J. Rock Mech. Geotech. Eng. 14 (3), 967–983.

Cervera, M., Chiumenti, M., 2006. Smeared crack approach: back to the original track. Int. J. Numer. Anal. Meth. Geomech. 30 (12), 1173–1199.

Chen, J.-S., Wu, C.-T., Yoon, S., et al., 2001. A stabilized conforming nodal integration for Galerkin meshfree methods. Int. J. Numer. Meth. Eng. 50 (2), 435–466.

Chen, J.-S., Hillman, M., Chi, S.-W., 2017. Meshfree methods: progress made after 20 years. J. Eng. Mech. 143 (4), 04017001.

Choo, J., Borja, R.I., 2015. Stabilized mixed finite elements for deformable porous media with double porosity. Comput. Meth. Appl. Mech. Eng. 293, 131–154.

Chowdhury, B., Dasari, G.R., Nogami, T., 2006. Laboratory study of liquefaction due to wave-seabed interaction. J. Geotech. Geoenviron. Eng. 132 (7), 842–851.

Cooper, M.R., Bromhead, E.N., Petley, D.J., et al., 1998. The Selborne cutting stability experiment. Geotechnique 48 (1), 83–101.

Cremonesi, M., Franci, A., Idelsohn, S., et al., 2020. A state of the art review of the particle finite element method (PFEM). Arch. Comput. Method E 27 (5), 1709–1735.

De Groot, M.B., Bolton, M.D., Foray, P., et al., 2006. Physics of liquefaction phenomena around marine structures. J. Waterw. Port Coast. Ocean Eng. 132 (4), 227–243.

Deborst, R., 1993. A generalization of J2-flow theory for polar continua. Comput. Meth. Appl. Mech. Eng. 103 (3), 347–362.

Feng, H., Cui, X.Y., Li, G.Y., 2016. A stable nodal integration method with strain gradient for static and dynamic analysis of solid mechanics. Eng. Anal. Bound. Elem. 62, 78–92.

Franci, A., Cremonesi, M., 2017. On the effect of standard PFEM remeshing on volume conservation in free-surface fluid flow problems. Comput. Part Mech. 4 (3), 331–343.

Gu, Y.T., Liu, G.R., 2001. A meshless local Petrov-Galerkin (MLPG) method for free and forced vibration analyses for solids. Comput. Mech. 27 (3), 188–198.

Haga, J.B., Osnes, H., Langtangen, H.P., 2012. On the causes of pressure oscillations in low-permeable and low-compressible porous media. Int. J. Numer. Anal. Meth. Geomech. 36 (12), 1507–1522.

Han, B., Zdravkovic, L., Kontoe, S., 2015. Stability investigation of the Generalised-alpha time integration method for dynamic coupled consolidation analysis. Comput. Geotech. 64, 83–95.

Hilber, H.M., Hughes, T.J.R., Taylor, R.L., 1977. Improved numerical dissipation for time integration algorithms in structural dynamics. Earthq. Eng. Struct. Dyn. 5 (3), 283–292.

Hillman, M., Chen, J.S., 2016. An accelerated, convergent, and stable nodal integration in Galerkin meshfree methods for linear and nonlinear mechanics. Int. J. Numer. Meth. Eng. 107 (7), 603–630.

Hughes, T.J., 2000. The Finite Element Method: Linear Static and Dynamic Finite Element Analysis. Dover Publications, New York.

Iwan, W.D., 1967. On a class of models for yielding behavior of continuous and composite systems. J. Appl. Mech. 34 (3), 612-&.

Jeng, D.S., Ye, J.H., Zhang, J.S., et al., 2013. An integrated model for the wave-induced seabed response around marine structures: model verifications and applications. Coast. Eng. 72, 1–19.

Jin, Y.F., Yin, Z.Y., 2022. Two-phase PFEM with stable nodal integration for large deformation hydromechanical coupled geotechnical problems. Comput. Meth. Appl. Mech. Eng. 392, 25.

Jin, Y.F., Yin, Z.Y., Yuan, W.H., 2020a. Simulating retrogressive slope failure using two different smoothed particle finite element methods: a comparative study. Eng. Geol. 279, 105870.

Jin, Y.F., Yuan, W.H., Yin, Z.Y., et al., 2020b. An edge-based strain smoothing particle finite element method for large deformation problems in geotechnical engineering. Int. J. Numer. Anal. Meth. Geomech. 44 (7), 923–941.

Kim, Y.H., Hossain, M.S., Wang, D., et al., 2015. Numerical investigation of dynamic installation of torpedo anchors in clay. Ocean Eng. 108, 820–832.

Kontoe, S., Zdravkovic, L., Potts, D.M., 2008. An assessment of time integration schemes for dynamic geotechnical problems. Comput. Geotech. 35 (2), 253–264.

Li, C., Borja, R.I., Regueiro, R.A., 2004. Dynamics of porous media at finite strain. Comput. Meth. Appl. Mech. Eng. 193 (36–38), 3837–3870.

Li, Y., Liu, G.R., 2019. A novel node-based smoothed finite element method with linear strain fields for static, free and forced vibration analyses of solids. Appl. Math Comput. 352, 30–58.

Liu, G.-R., 2009. Meshfree Methods: Moving Beyond the Finite Element Method. CRC Press, Boca Raton.

Liu, G.R., Nguyen-Thoi, T., Nguyen-Xuan, H., et al., 2009a. A node-based smoothed finite element method (NS-FEM) for upper bound solution to solid mechanics problems. Comput. Struct. 87 (1–2), 14–26.

Liu, G.-R., Trung, N., 2016. Smoothed Finite Element Methods. CRC Press, Boca Raton.

Liu, G.-R., Nguyen-Thoi, T., Lam, K.Y., 2009b. An edge-based smoothed finite element method (ES-FEM) for static, free and forced vibration analyses of solids. J. Sound Vibr. 320 (4–5), 1100–1130.

Liu, G.R., Nguyen-Xuan, H., Nguyen-Thoi, T., 2010. A theoretical study on the smoothed FEM (S-FEM) models: properties, accuracy and convergence rates. Int. J. Numer. Meth. Eng. 84 (10), 1222–1256.

Markert, B., Heider, Y., Ehlers, W., 2010. Comparison of monolithic and splitting solution schemes for dynamic porous media problems. Int. J. Numer. Meth. Eng. 82 (11), 1341–1383.

Mira, P., Pastor, M., Li, T., et al., 2003. A new stabilized enhanced strain element with equal order of interpolation for soil consolidation problems. Comput. Meth. Appl. Mech. Eng. 192 (37–38), 4257–4277.

Monforte, L., Arroyo, M., Carbonell, J.M., et al., 2017a. Numerical simulation of undrained insertion problems in geotechnical engineering with the Particle Finite Element Method (PFEM). Comput. Geotech. 82, 144–156.

Monforte, L., Carbonell, J.M., Arroyo, M., et al., 2017b. Performance of mixed formulations for the particle finite element method in soil mechanics problems. Comput. Part Mech. 4 (3), 269–284.

Monforte, L., Arroyo, M., Carbonell, J.M., et al., 2018. Coupled effective stress analysis of insertion problems in geotechnics with the Particle Finite Element Method. Comput. Geotech. 101, 114–129.

Monforte, L., Navas, P., Carbonell, J.M., et al., 2019. Low-order stabilized finite element for the full Biot formulation in soil mechanics at finite strain. Int. J. Numer. Anal. Meth. Geomech. 43 (7), 1488–1515.

Mory, M., Michallet, H., Bonjean, D., et al., 2007. A field study of momentary liquefaction caused by waves around a coastal structure. J. Waterw. Port Coast Ocean Eng.-ASCE 133 (1), 28–38.

Moutsanidis, G., Koester, J.J., Tupek, M.R., et al., 2020. Treatment of near-incompressibility in meshfree and immersed-particle methods. Comput. Part Mech. 7 (2), 309–327.

Newmark, N.M., 1965. Effects of earthquakes on dams and embankments. Geotechnique 15 (2), 139–160.

Nguyen-Xuan, H., Liu, G.R., 2013. An edge-based smoothed finite element method softened with a bubble function (bES-FEM) for solid mechanics problems. Comput. Struct. 128, 14–30.

Onate, E., 2000. A stabilized finite element method for incompressible viscous flows using a finite increment calculus formulation. Comput. Meth. Appl. Mech. Eng. 182 (3–4), 355–370.

Pastor, H., Li, T., Liu, X., et al., 2000. A fractional step algorithm allowing equal order of interpolation for coupled analysis of saturated soil problems. Mech. Cohesive-Frict. Mater. 5 (7), 511–534.
Pavlatos, G.D., Beskos, D.E., 1994. Dynamic elastoplastic analysis by BEM/FEM. Eng. Anal. Bound. Elem. 14 (1), 51–63.
Preisig, M., Prevost, J.H., 2011. Stabilization procedures in coupled poromechanics problems: a critical assessment. Int. J. Numer. Anal. Meth. Geomech. 35 (11), 1207–1225.
Puso, M.A., Chen, J.S., Zywicz, E., et al., 2008. Meshfree and finite element nodal integration methods. Int. J. Numer. Meth. Eng. 74 (3), 416–446.
Sabetamal, H., Nazem, M., Carter, J.P., et al., 2014. Large deformation dynamic analysis of saturated porous media with applications to penetration problems. Comput. Geotech. 55, 117–131.
Sabetamal, H., Nazem, M., Sloan, S.W., et al., 2016. Frictionless contact formulation for dynamic analysis of nonlinear saturated porous media based on the mortar method. Int. J. Numer. Anal. Meth. Geomech. 40 (1), 25–61.
Sabetamal, H., Carter, J.P., Zhang, X., et al., 2021. Coupled analysis of full flow penetration problems in soft sensitive clays. Comput. Geotech. 133, 13.
Sabetamal, H., Sheng, D.C., Carter, J.P., 2022. Coupled hydro-mechanical modelling of unsaturated soils; numerical implementation and application to large deformation problems. Comput. Geotech. 152, 24.
Salgado, R., Bisht, V., 2021. Advances in the solution of geotechnical boundary-value problems. Comput. Geotech. 138, 11.
Soga, K., Alonso, E., Yerro, A., et al., 2016. Trends in large-deformation analysis of landslide mass movements with particular emphasis on the material point method. Geotechnique 66 (3), 248–273.
Sun, W.C., Ostien, J.T., Salinger, A.G., 2013. A stabilized assumed deformation gradient finite element formulation for strongly coupled poromechanical simulations at finite strain. Int. J. Numer. Anal. Meth. Geomech. 37 (16), 2755–2788.
Vo-Minh, T., Nguyen-Son, L., 2021. A stable node-based smoothed finite element method for stability analysis of two circular tunnels at different depths in cohesive-frictional soils. Comput. Geotech. 129, 103865.
Wang, Z.-Y., Jin, Y.-F., Yin, Z.-Y., et al., 2022a. A novel coupled NS-PFEM with stable nodal integration and polynomial pressure projection for geotechnical problems. Int. J. Numer. Anal. Meth. Geomech. 46 (13), 2535–2560.
Wang, Z.-Y., Jin, Y.-F., Yin, Z.-Y., et al., 2022b. Overcoming volumetric locking in stable node-based smoothed particle finite element method with cubic bubble function and selective integration. Int. J. Numer. Meth. Eng. 123 (24), 6148–6169.
Wang, L., Zhang, X., Tinti, S., 2021a. Large deformation dynamic analysis of progressive failure in layered clayey slopes under seismic loading using the particle finite element method. Acta Geotech. 16 (8), 2435–2448.
Wang, L., Zhang, X., Zhang, S., et al., 2021b. A generalized Hellinger-Reissner variational principle and its PFEM formulation for dynamic analysis of saturated porous media. Comput. Geotech. 132, 12.
Wei, H.Y., Chen, J.S., Hillman, M., 2016. A stabilized nodally integrated meshfree formulation for fully coupled hydro-mechanical analysis of fluid-saturated porous media. Comput. Fluids 141, 105–115.
Wei, H.Y., Chen, J.S., Beckwith, F., et al., 2020. A naturally stabilized semi-Lagrangian meshfree formulation for multiphase porous media with application to landslide modeling. J. Eng. Mech. 146 (4), 04020012.
White, J.A., Borja, R.I., 2008. Stabilized low-order finite elements for coupled solid-deformation/fluid-diffusion and their application to fault zone transients. Comput. Meth. Appl. Mech. Eng. 197 (49–50), 4353–4366.
Wood, W.L., Bossak, M., Zienkiewicz, O.C., 1980. An alpha-modification of Newmark method. Int. J. Numer. Meth. Eng. 15 (10), 1562–1566.
Xu, C.S., Song, J., Du, X.L., et al., 2017a. A completely explicit finite element method for solving dynamic u-p equations of fluid-saturated porous media. Soil Dyn. Earthq. Eng. 97, 364–376.
Xu, C.S., Song, J., Du, X.L., et al., 2017b. A local artificial-boundary condition for simulating transient wave radiation in fluid-saturated porous media of infinite domains. Int. J. Numer. Meth. Eng. 112 (6), 529–552.
Yang, H., Cui, X.Y., Li, S., et al., 2019. A stable node-based smoothed finite element method for metal forming analysis. Comput. Mech. 63 (6), 1147–1164.
Ye, J., Jeng, D.S., 2011. Effects of bottom shear stresses on the wave-induced dynamic response in a porous seabed: PORO-WSSI (shear) model. Acta Mech. Sin. 27 (6), 898–910.
Ye, J.H., Jeng, D.S., 2012. Response of porous seabed to nature loadings: waves and currents. J. Eng. Mech. 138 (6), 601–613.
Yerro, A., Alonso, E.E., Pinyol, N.M., 2015. The material point method for unsaturated soils. Geotechnique 65 (3), 201–217.
Yuan, W.H., Wang, B., Zhang, W., et al., 2019. Development of an explicit smoothed particle finite element method for geotechnical applications. Comput. Geotech. 106, 42–51.
Yuan, W.H., Zhu, J.X., Liu, K., et al., 2022. Dynamic analysis of large deformation problems in saturated porous media by smoothed particle finite element method. Comput. Meth. Appl. Mech. Eng. 392, 29.
Zeng, W., Liu, G.R., 2018. Smoothed finite element methods (S-FEM): an overview and recent developments. Arch. Comput. Method E 25 (2), 397–435.
Zhang, X., Krabbenhoft, K., Pedroso, D.M., et al., 2013. Particle finite element analysis of large deformation and granular flow problems. Comput. Geotech. 54, 133–142.
Zhang, X., Krabbenhoft, K., Sheng, D.C., et al., 2015. Numerical simulation of a flow-like landslide using the particle finite element method. Comput. Mech. 55 (1), 167–177.
Zhang, X., Sheng, D.C., Sloan, S.W., et al., 2016a. Second-order cone programming formulation for consolidation analysis of saturated porous media. Comput. Mech. 58 (1), 29–43.
Zhang, X., Ding, Y.T., Sheng, D.C., et al., 2016b. Quasi-static collapse of two-dimensional granular columns: insight from continuum modelling. Granul. Matter 18 (3).
Zhang, X., Wang, L., Krabbenhoft, K., et al., 2020. A case study and implication: particle finite element modelling of the 2010 Saint-Jude sensitive clay landslide. Landslides 17 (5), 1117–1127.
Zhang, Q., Yan, X., Shao, J.L., 2021. Fluid flow through anisotropic and deformable double porosity media with ultra-low matrix permeability: a continuum framework. J. Pet. Sci. Eng. 200, 11.
Zhang, Q., Yan, X., Li, Z.H., 2022a. A mathematical framework for multiphase poromechanics in multiple porosity media. Comput. Geotech. 146, 104728.
Zhang, Q., Wang, Z.-Y., Jin, Y.-F., et al., 2022b. A novel stabilized NS-FEM formulation for anisotropic double porosity media. Comput. Meth. Appl. Mech. Eng. 401, 115666.
Zhang, W., Yuan, W.H., Dai, B.B., 2018. Smoothed particle finite-element method for large-deformation problems in geomechanics. Int. J. Geomech. 18 (4), 04018010.
Zhao, Y., Borja, R.I., 2021. Anisotropic elastoplastic response of double-porosity media. Comput. Meth. Appl. Mech. Eng. 380, 32.
Zhao, Y.D., Choo, J., 2020. Stabilized material point methods for coupled large deformation and fluid flow in porous materials. Comput. Meth. Appl. Mech. Eng. 362, 112742.
Zienkiewicz, O.C., Shiomi, T., 1984. Dynamic behavior of saturated porous media - the generalized biot formulation and its numerical solution. Int. J. Numer. Anal. Meth. Geomech. 8 (1), 71–96.
Zienkiewicz, O.C., Chang, C.T., Bettess, P., 1980. Drained, undrained, consolidating and dynamic behavior assumptions in soils. Geotechnique 30 (4), 385–395.